Numerical Investigation of Thermal Convection with a Tilted Magnetic Field

by

Justin A. Nicoski

A thesis submitted to the

University of Colorado in partial fulfillment

of the requirements for Departmental Honors

Department of Physics

2020

Defense Committee

Prof. Michael Calkins - Advisor, Department of Physics

Prof. Paul Beale - Honors Council Representative, Department of Physics

Prof. Ben Brown - Outside Reader, Department of Astrophysical and Planetary Sciences

Defense conducted April 2, 2020

This thesis entitled:
Numerical Investigation of Thermal Convection with a Tilted Magnetic Field
written by Justin A. Nicoski
has been approved for the Department of Physics

Prof. Michael Calkins

Prof. Paul Beale

Prof. Ben Brown

Date _____

The final copy of this thesis has been examined by the signatories, and we find that both the content and the form meet acceptable presentation standards of scholarly work in the above mentioned discipline.

Nicoski, Justin A. (B.A., Physics)

Numerical Investigation of Thermal Convection with a Tilted Magnetic Field

Thesis directed by Prof. Michael Calkins

Rayleigh-Bénard convection is investigated numerically in the presence of a uniform magnetic field tilted with respect to the vertical. The tilt of the imposed magnetic field is fixed at 45°. The buoyancy force and the strength of the magnetic field are varied, as characterized by the Rayleigh number (Ra) and Chandrasekhar number (Q), respectively. The onset of convection consists of longitudinal rolls with their axes orientated parallel to the imposed magnetic field. As Q increases, the rolls become thinner and persist over a decreasing range of supercritical values of Ra. A mean flow characterized by jets forms near the onset of convection and persists over a wide range of Rayleigh numbers. The mean flow causes the y-velocity to be the dominant component of velocity. For $Q = 2 \times 10^3$, the mean flow dissipates at sufficiently large values of Ra. For simulations with sufficiently large Q over a range of Ra, relaxation oscillations are observed. Relaxation oscillations are characterized by large changes of the Nusselt number and Reynolds number in time, corresponding to the growth and decay of the mean flow. Columnar-like fluid structures are observed to align with the direction of the imposed magnetic field for large values of Q. An energy dissipation relation is used to determine the relative sizes of the viscous and Ohmic dissipation where it is found that the Ohmic dissipation remains larger than the viscous dissipation for the parameter space of Q and Ra studied in this paper. The flow speeds and heat transport for convection in tilted and vertical magnetic fields are compared. The flow speeds for convection in a tilted magnetic field are larger than the flow speeds for convection in a vertical magnetic field for a wide range of Ra due to the presence of a mean flow. The heat transport is found to be smaller for convection in a tilted magnetic field than for convection in a vertical magnetic field, despite both cases having identical supercritical Rayleigh numbers.

Acknowledgements

This research paper would not have been possible without the guidance of Professor Calkins, to whom I am deeply grateful. He has provided a constant source of inspiration and given direction to my research. Many thanks to Professor Calkins for continuing to support me through all the drafts of this paper, of which there were many. I would also like to thank graduate student Ming Yan for introducing me to the code required for this research and for providing me with useful scripts. And, of course, I cannot forget my dear sister who has labored many hours with me late at night, reading through my honors thesis and correcting many typos.

This work utilized resources from the University of Colorado Boulder Research Computing Group, which is supported by the National Science Foundation (awards ACI-1532235 and ACI-1532236), the University of Colorado Boulder, and Colorado State University.

Contents

Chapter

1 Introduction 1

2 Methods 4

3 Results 8

3.1 Summary of cases 8

3.2 Overview of flow regimes 10

3.3 Mean flow character 11

3.3.1 Mean flow formation 11

3.3.2 Characteristics of the mean flow 13

3.3.3 Mean flow equation 14

3.3.4 Horizontally averaged velocities and forces 18

3.3.5 Relaxation oscillations 20

3.4 Balances in the governing equations 22

3.5 Influence of the aspect ratio 25

3.6 Reynolds number scaling 27

3.7 Tilt of convective cells along the magnetic field 28

3.8 Heat transport 30

3.9 Comparison to convection in a vertical magnetic field 34

4 Conclusion 36

Bibliography 38

Tables

Table

2.1 Summary of critical values for the Chandrasekhar numbers used in this paper. . . . 5

3.1 Data collected for the simulations studied in this paper. 9

Figures

Figure

2.1 (a) The geometry of the system being studied. (b) The motion of the fluid at the onset of convection. 7

3.1 Volumetric renderings of the temperature fluctuation for three flow regimes. 10

3.2 Fluid velocity for Ra slightly beyond the onset of convection. 12

3.3 Fourier spectra of fluid velocity for Ra slightly beyond the onset of convection. . . . 12

3.4 The structure of the mean flow. 13

3.5 Profiles of the y-velocity averaged along the y-direction for the simulation $Q = 2 \times 10^6$, $Ra = 5 \times 10^7$. 14

3.6 Plots of the terms in the mean flow equation at one instant in time. 15

3.7 Plots of additional terms in the mean flow equation at one instant in time. 15

3.8 Plots of the terms in the mean flow equation for $Q = 2 \times 10^3$, $Q = 2 \times 10^5$, and $Q = 2 \times 10^6$. 16

3.9 Horizontal average and horizontal rms of the x-component of velocity averaged in time as a function of the height of the simulation domain. Cases from $Q = 2 \times 10^3$. . 17

3.10 Horizontal average and horizontal rms of the y-component of velocity averaged in time as a function of the height of the simulation domain. Cases from $Q = 2 \times 10^3$. . 18

3.11 The terms from the horizontally averaged Navier-Stokes equation at one instant in time. 18

3.12 Plots of the Reynolds number and Nusselt number for the relaxation oscillation simulation $Q = 2 \times 10^5$, $Ra = 1.5 \times 10^7$. 20

3.13 Plots depicting how the x-velocity and y-velocity in the xy-plane change in time for a simulation undergoing relaxation oscillations. 20

3.14 Plots showing how the terms of the mean flow equation change in time for a simulation undergoing relaxation oscillations. 21

3.15 Plots showing a horizontal rms of the vertical forces from the Navier-Stokes equation at one instant in time for different flow regimes. 23

3.16 Plots showing a horizontal rms of the horizontal forces from the Navier-Stokes equation at one instant in time for different flow regimes. 24

3.17 Plots showing a horizontal rms of temperature terms at one instant in time for different flow regimes. 26

3.18 Plots depicting the Reynolds number as a function of the aspect ratio used. 27

3.19 Kinetic energy ratios from the three velocity components averaged in time. 28

3.20 Plots depicting the Reynolds number for various Rayleigh numbers and Chandrasekhar numbers. 29

3.21 Plot showing the temperature fluctuation and the velocity in the xz-plane for the simulation $Q = 2 \times 10^5$, $Ra = 6 \times 10^6$. 30

3.22 Plots of the Nusselt number for various Rayleigh and Chandrasekhar numbers. . . . 31

3.23 The mean temperature $\overline{T}$ as a function of the height of the simulation domain for $Q = 2 \times 10^3$. 31

3.24 Dissipation ratios for $Q = 2 \times 10^3$ and $Q = 2 \times 10^5$. 31

3.25 The horizontally averaged and time averaged dissipation plotted as a function of the vertical height of the simulation domain. 32

3.26 Comparison of the Reynolds number and the Nusselt number between convection in a vertical magnetic field and convection in a tilted magnetic field. 34

Chapter 1

Introduction

Convection of electrically conducting fluids under the influence of magnetic fields is common in both planetary and stellar systems. In sun-like stars, fusion within the core creates a temperature gradient leading to convection in the outer layer. The presence of magnetic fields can have a significant influence on the resulting convection. One dramatic example of this is sunspots, where powerful vertical magnetic fields near the center of the sunspot, and oblique magnetic fields near the edges, disrupt the transfer of heat through convection and cause the surface to visually appear darker [1].

The equations describing the motion of fluids have analytic solutions only in the linear and weakly nonlinear regime, so numerical modeling is an important method for studying fluid flow, along with experimental studies. A commonly studied numerical setup consists of a horizontally infinite layer of fluid with depth H that is heated from below and cooled from above. A uniform gravitational field $\mathbf{g} = -g\hat{z}$ is imposed, and for sufficient heating, this system undergoes convection. This setup is known as Rayleigh-Bénard convection. Nondimensionalizing the equations of motion reduces the number of independent control parameters. Doing so yields the Rayleigh number and the Prandtl number, Pr, defined as

$$Ra = \frac{\alpha g \Delta T H^3}{\kappa \nu}, \quad Pr = \frac{\nu}{\kappa}, \tag{1.1}$$

where α is the thermal expansion coefficient, g is the gravitational acceleration, ΔT is the temperature difference between the top and bottom surfaces, κ is the thermal diffusivity, and ν is

the kinematic viscosity. The Rayleigh number measures how strongly the system is forced. The Prandtl number is a property of the fluid and, in many systems, such as stars and liquid metals, the Prandtl number is much less than one. The value of the Prandtl number is set to unity in this paper because low values of the Prandtl number are more computationally expensive, and the goal of this paper was to simulate convection for large Rayleigh numbers.

In the presence of a magnetic field, new terms added to the equations of motion give rise to the new non-dimensional parameters

$$Q = \frac{\sigma B_0^2 H^2}{\rho \nu}, \quad Pr_m = \sigma \nu \mu, \tag{1.2}$$

where B_0 is the strength of the magnetic field, ρ is the density of the fluid, σ is the electric conductivity of the fluid, μ is the magnetic permeability, Q is the Chandrasekhar number, and Pr_m is the magnetic Prandtl number. The Chandrasekhar number is related to the magnetic field strength; larger values of Q tend to inhibit the convection. The magnetic Prandtl number is a property of the fluid. In natural systems such as stars, the Chandrasekhar numbers and the Rayleigh numbers tend to be quite large; the Rayleigh number is of the order $Ra = O(10^{18})$ in stars [2]. The Chandrasekhar number of the Earth's core is known to be large with a value of the order $Q = O(10^{15})$ [3]. However, numerical simulations cannot yet achieve values this large due to the computational cost required, which makes studying these systems difficult.

Letting θ be the angle of the magnetic field from the vertical, the cases of a vertical magnetic field and a horizontal magnetic field are the limits as $\theta \to 0°$ and $\theta \to 90°$, respectively. The vertical magnetic field has been studied for Chandrasekhar numbers as large as $Q = 10^8$ [4]. The horizontal magnetic field has been studied for Chandrasekhar numbers up to 10^6 [5]. In most systems the magnetic field is self-generated, leading to a complex spatiotemporal structure that makes it difficult to understand how the field influences the fluid motions. Previous studies of magnetoconvection with a tilted magnetic field are more limited. A study of the effects of a tilted magnetic field on convection was carried out in two dimensions for $Q = 10^3$ [6]. A different study of magnetoconvection included a section on three-dimensional convection influenced by a tilted

magnetic field for $Q = 1.333 \times 10^3$ [7].

While the non-dimensional parameters that characterize natural systems such as stars and planets are too extreme for numerical simulations, simulations across a wide range of parameter space may still offer insight into these convective processes. In this paper, the effects of a tilted magnetic field on convection are studied for a large range of both Chandrasekhar numbers and Rayleigh numbers.

Chapter 2

Methods

Rayleigh-Bénard convection is studied with the Boussinesq approximation. A uniform, externally imposed magnetic field is tilted at an angle of 45°. We use the quasi-static approximation, which is valid when the induced magnetic field is small compared to the imposed magnetic field. This approximation assumes both the induced magnetic field and the magnetic Prandtl number are of order ϵ, so the magnetic Prandtl number does not appear in the equations of motion. In this paper, a bar will denote a horizontal average and is given by

$$\overline{f} = \frac{1}{L_x L_y} \int_0^{L_y} \int_0^{L_x} f dx dy, \tag{2.1}$$

where L_x is the length of the simulation domain in the x-direction and L_y is the length of the simulation domain in the y-direction. The fluctuating value of a parameter is then defined to be $f' = f - \overline{f}$. With this, the non-dimensional system of equations is given by

$$\frac{\partial \mathbf{u}}{\partial t} + \mathbf{u} \cdot \nabla \mathbf{u} = -\nabla P + \frac{Ra}{Pr} T' \hat{z} + \nabla^2 \mathbf{u} + Q \hat{\boldsymbol{\eta}} \cdot \nabla \mathbf{b}, \tag{2.2}$$

$$\left(\frac{\partial}{\partial t} - \frac{1}{Pr} \frac{\partial^2}{\partial z^2} \right) \overline{T} = -\frac{\partial}{\partial z} \left(\overline{wT'} \right), \tag{2.3}$$

$$\left(\frac{\partial}{\partial t} - \frac{1}{Pr} \nabla^2 \right) T' = -\mathbf{u} \cdot \nabla T' - w \frac{\partial \overline{T}}{\partial z} + \frac{\partial}{\partial z} \left(\overline{wT'} \right), \tag{2.4}$$

$$0 = \hat{\boldsymbol{\eta}} \cdot \nabla \mathbf{u} + \nabla^2 \mathbf{b}, \tag{2.5}$$

$$\nabla \cdot \mathbf{u} = 0 \qquad \nabla \cdot \mathbf{b} = 0, \tag{2.6}$$

where $\mathbf{u} = (u, v, w)$ is the velocity of the fluid, P is the reduced pressure, θ is the angle of the magnetic field, $\mathbf{b}$ is the induced magnetic field, T is the temperature, and $\hat{\boldsymbol{\eta}}$ is a unit vector

Q	Ra_c	λ_c	k_c
2×10^3	1.5207×10^4	1.1054	5.6842
2×10^5	1.0784×10^6	0.48956	12.8343
2×10^6	1.0281×10^7	0.33100	18.9823

Table 2.1: Summary of critical values for the Chandrasekhar numbers used in this paper.

pointing along the imposed magnetic field. These equations were nondimensionalized using

$$\mathbf{u} = \frac{H}{\nu}\widetilde{\mathbf{u}}, \quad x_i = \frac{1}{H}\widetilde{x_i}, \quad t = \frac{\nu}{H^2}\widetilde{t}, \quad \mathbf{b} = \frac{1}{B_0}\widetilde{\mathbf{b}}, \quad T' = \frac{1}{\Delta T}\widetilde{T'}, \tag{2.7}$$

where the tildes denote the dimensional forms of the variables. Several important terms in the Navier-Stokes equation (equation 2.2) are as follows: $F_a = \mathbf{u} \cdot \nabla \mathbf{u}$ is the advection term, $F_p = -\nabla P$ is the pressure force, $F_b = (Ra/Pr)T'\hat{z}$ is the buoyancy force, $F_v = \nabla^2 \mathbf{u}$ is the viscous force, and $F_l = Q\hat{\boldsymbol{\eta}} \cdot \nabla \mathbf{b}$ is the Lorentz force.

The geometry of the problem is that of a rectangular box with a magnetic field held at an angle of θ as shown in figure 2.1 (a). The boundary conditions for the velocity are such that the vertical component of velocity and the tangential stresses are zero at the top and bottom surfaces, giving

$$w = 0, \qquad \frac{\partial u}{\partial z} = 0, \qquad \frac{\partial v}{\partial z} = 0, \tag{2.8}$$

at the boundaries. The boundary condition used for the electromagnetic equations is one of an insulator at the lower and upper boundaries, meaning that the vertical component of current density is zero at the top and bottom surfaces. The other four sides of the simulation domain are treated as periodic, so no boundary conditions are needed on these sides.

From linear theory, it can be shown that at the onset of convection

$$Ra_m(k) = \frac{\pi^2 + k^2}{k^2}[(\pi^2 + k^2)^2 + Q\cos^2(\theta)\pi^2], \tag{2.9}$$

where Ra_m is the marginal Rayleigh number and k is the wavenumber [8]. Letting the value of k that minimizes this expression be k_c, the critical Rayleigh number is given by $Ra_c = Ra_m(k_c)$, where the critical Rayleigh number is the Rayleigh number at which convection starts. The critical wavelength is defined as $\lambda_c = 2\pi/k_c$. A summary of critical values is provided in table 2.1. Asymptotically,

the critical values approach [8]

$$Ra_c = Q\cos^2(\theta)\pi^2, \qquad k_c = \pi\left(\frac{Q\cos^2(\theta)}{2\pi^2}\right)^{\frac{1}{6}}, \qquad Q \to \infty. \tag{2.10}$$

Since all of the simulations run had the same length for the horizontal sides of the simulation domain, it is useful to define the aspect ratio as

$$\Gamma = \frac{L}{H}, \tag{2.11}$$

where L is the horizontal side length of the simulation domain. Unless otherwise stated, the size of the simulation domain is given by $(L_x, L_y, H) = (10\lambda_c, 10\lambda_c, 1)$, or $\Gamma = 10\lambda_c$. The form of convection at the onset takes the form of rolls aligned along the x-axis as shown in figure 2.1 (b). The onset of convection is steady for the parameter space studied in this paper.

In solving the governing equations, the code uses a toroidal-poloidal decomposition so that the velocity and magnetic field exactly satisfy the solenoidal conditions for the velocity and magnetic field. Pseudo-spectral methods are used in which data is represented in the horizontal directions by Fourier series and in the vertical direction by Chebyshev polynomials. The time stepping scheme consists of a third-order implicit-explicit Runge-Kutta method.

Two important outputs from the code include the Nusselt number and the Reynolds number. The Nusselt number measures the heat transported vertically and is unity when the heat transport is accomplished solely by conduction. Then, as advection starts to transport heat, the Nusselt number increases. The Reynolds number is a measure of the average flow speed of the fluid. The Nusselt number and Reynolds number are defined as

$$Nu = 1 + Pr\langle wT'\rangle, \tag{2.12}$$

and

$$Re = \langle u^2 + v^2 + w^2\rangle^{\frac{1}{2}}, \tag{2.13}$$

where $\langle\rangle$ denotes a volume and time average.

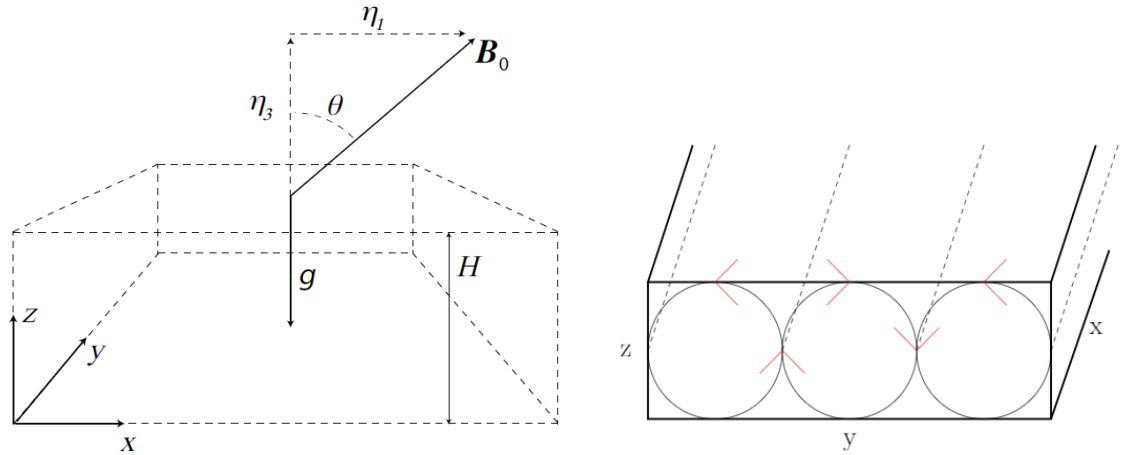

(a) (b)

Figure 2.1: (a) The geometry of the problem studied. H is the height of the simulation domain, $\mathbf{g}$ is the gravitational acceleration, $\mathbf{B}_0$ is the imposed magnetic field, θ is the angle of the imposed magnetic field, and η_1 and η_3 are the components of a unit vector pointing along $\mathbf{B}_0$. (b) Convection first takes the form of rolls as predicted in linear theory [8]. The red arrows represent the motion of the fluid. Note that there is no fluid motion along the x-direction. The fluid extends infinitely along the x and y directions and the magnetic field has equal components in the x and z directions.

Chapter 3

Results

3.1 Summary of cases

Simulations were carried out for Chandrasekhar numbers of $Q = 2 \times 10^3$, 2×10^5, and 2×10^6. Rayleigh numbers up to $Ra = 100Ra_c$ were investigated. Collected data is summarized in table 3.1. These values of the Chandrasekhar number were chosen so that the value of the critical Rayleigh number would be the same as the critical Rayleigh number in a study of convection in a vertical magnetic field [4]. This makes comparisons of the data between the vertical and tilted magnetic field easier.

The resolution in the horizontal directions is chosen so that, in spectral space, there are more than two orders of magnitude between the leading-order frequencies and the highest frequencies. A higher resolution in the z-direction is needed for convection in a tilted magnetic field than in a vertical magnetic field. This higher resolution requirement is due to the fluid structures aligning themselves along the imposed magnetic field and the formation of a thin boundary layer for convection in a tilted magnetic field.

The simulations were run on the Summit Supercomputer. The average run used approximately 100 CPUs, and the most expensive simulations used approximately 700 CPUs. Each run generally required 10-24 hours wall-clock time, and most simulations required multiple restarts to reach equilibrium. The most expensive simulations required a total run time of approximately 10^5 CPU hours.

Q	Ra	Nu	Re	Δt	$N_x \times N_y \times N_z$
2×10^3	1.53×10^4	1.012 ± 0.000	0.822 ± 0.000	10^{-3}	$96 \times 96 \times 48$
2×10^3	2×10^4	1.30 ± 0.03	5.05 ± 0.19	10^{-3}	$96 \times 144 \times 48$
2×10^3	2.5×10^4	1.54 ± 0.04	8.29 ± 0.24	10^{-3}	$144 \times 144 \times 48$
2×10^3	4×10^4	2.19 ± 0.04	17.86 ± 0.24	5×10^{-4}	$144 \times 192 \times 48$
2×10^3	6×10^4	2.83 ± 0.05	30.98 ± 0.35	2×10^{-4}	$192 \times 288 \times 72$
2×10^3	1×10^5	3.75 ± 0.05	54.80 ± 0.37	1×10^{-4}	$288 \times 288 \times 144$
2×10^3	2×10^5	5.22 ± 0.07	103.43 ± 0.71	4×10^{-5}	$288 \times 384 \times 144$
2×10^3	4×10^5	7.06 ± 0.09	179.71 ± 0.79	4×10^{-5}	$384 \times 576 \times 144$
2×10^3	6×10^5	8.38 ± 0.09	229.58 ± 1.90	2×10^{-5}	$576 \times 576 \times 144$
2×10^3	1×10^6	10.35 ± 0.11	285.17 ± 2.17	1×10^{-5}	$768 \times 768 \times 192$
2×10^3	2×10^6	13.42 ± 0.12	214.17 ± 2.16	5×10^{-6}	$768 \times 768 \times 288$
2×10^5	1.1×10^6	1.024 ± 0.006	2.11 ± 0.29	10^{-5}	$96 \times 144 \times 72$
2×10^5	1.3×10^6	1.17 ± 0.01	8.16 ± 0.41	10^{-5}	$96 \times 144 \times 72$
2×10^5	1.5×10^6	1.31 ± 0.02	13.93 ± 0.53	10^{-5}	$144 \times 192 \times 72$
2×10^5	1.7×10^6	1.46 ± 0.03	20.68 ± 0.61	10^{-5}	$144 \times 192 \times 72$
2×10^5	2×10^6	1.71 ± 0.03	32.61 ± 0.64	10^{-5}	$192 \times 192 \times 72$
2×10^5	2.2×10^6	1.87 ± 0.03	41.31 ± 0.60	10^{-5}	$192 \times 192 \times 72$
2×10^5	2.5×10^6	2.09 ± 0.04	55.85 ± 0.67	10^{-5}	$192 \times 192 \times 72$
2×10^5	3×10^6	2.45 ± 0.04	81.53 ± 0.76	10^{-5}	$192 \times 288 \times 96$
2×10^5	4×10^6	3.11 ± 0.07	134.82 ± 1.32	10^{-5}	$288 \times 384 \times 96$
2×10^5	6×10^6	4.24 ± 0.13	240.66 ± 1.88	10^{-5}	$288 \times 384 \times 144$
2×10^5	8×10^6	5.18 ± 0.18	343.92 ± 2.16	10^{-5}	$576 \times 576 \times 144$
2×10^5	1×10^7	6.55 ± 0.27	323.43 ± 72.48	5×10^{-6}	$576 \times 576 \times 192$
2×10^5	1.5×10^7	8.30 ± 0.38	548.14 ± 114.34	2×10^{-6}	$576 \times 576 \times 288$
2×10^5	3×10^7	12.67 ± 0.40	921.73 ± 195.51	2×10^{-6}	$576 \times 768 \times 288$
2×10^6	1.1×10^7	1.07 ± 0.01	6.75 ± 0.37	10^{-6}	$96 \times 144 \times 144$
2×10^6	1.3×10^7	1.21 ± 0.01	16.17 ± 0.75	10^{-6}	$144 \times 192 \times 144$
2×10^6	1.5×10^7	1.37 ± 0.02	29.24 ± 0.91	10^{-6}	$144 \times 192 \times 144$
2×10^6	2×10^7	1.81 ± 0.03	73.14 ± 1.03	10^{-6}	$144 \times 288 \times 144$
2×10^6	2.5×10^7	2.25 ± 0.04	125.88 ± 1.29	10^{-6}	$192 \times 288 \times 144$
2×10^6	3×10^7	$2.64 \pm .06$	184.21 ± 1.91	10^{-6}	$288 \times 288 \times 144$
2×10^6	4×10^7	$3.41 \pm .07$	305.61 ± 2.88	10^{-6}	$384 \times 384 \times 192$
2×10^6	5×10^7	$4.14 \pm .10$	422.72 ± 5.20	10^{-6}	$384 \times 576 \times 192$
2×10^6	7×10^7	$5.47 \pm .14$	663.53 ± 3.17	10^{-6}	$576 \times 768 \times 288$

Table 3.1: Data collected for $\Gamma = 10\lambda_c$. The errors shown are the standard deviation in time. N_x, N_y, and N_z are the number of node points along the x-direction, y-direction, and z-direction, respectively. Δt is the time step used in the simulation.

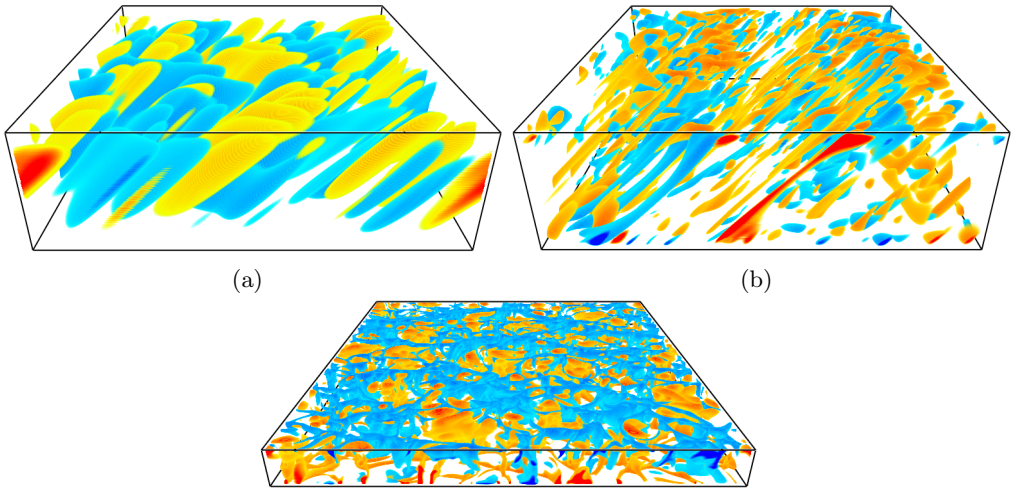

(a) (b)

(c)

Figure 3.1: Volumetric renderings of the temperature fluctuation for three flow regimes. The red and yellow represent warmer fluid while the blue represents cooler fluid. The aspect ratio used for these three-dimensional renderings was $\Gamma = 10\lambda_c$. These volumetric renderings were made using Vapor [9]. (a) The cellular regime with $Q = 2 \times 10^6$, $Ra = 1.5 \times 10^7$. (b) The columnar regime with $Q = 2 \times 10^6$, $Ra = 7 \times 10^7$. (c) The turbulent regime with $Q = 2 \times 10^3$, $Ra = 2 \times 10^6$.

3.2 Overview of flow regimes

Here an overview of the flow regimes is provided as the Rayleigh number and Chandrasekhar number are varied. At the onset of convection, steady rolls form as predicted by linear theory [8]. As the Rayleigh number is increased past the critical Rayleigh number, a mean flow begins to develop along the y-direction at approximately $Ra = 1.012Ra_c$ for $Q = 2 \times 10^6$. The mean flow is the size of the entire simulation domain, and as the Rayleigh number is increased, the strength of the mean flow increases as well. For a Chandrasekhar number of $Q = 2 \times 10^3$ and a Rayleigh number of the order $Ra = 10^2 Ra_c$, the mean flow dissipates and the convection becomes turbulent. This regime was not observed for higher values of Q due to computational constraints. For $Q = 2 \times 10^5$, the mean flow undergoes large scale oscillations for Rayleigh numbers of $Ra \gtrsim 10Ra_c$ and persists through the largest Rayleigh number studied—$Ra = 30Ra_c$. Relaxation oscillations are characterized by large variations of the Reynolds number and Nusselt number in time. Relaxation oscillations are not observed for $Q = 2 \times 10^3$, suggesting that a sufficiently strong magnetic field is required for

relaxation oscillations to occur.

In addition to these large scale flows, there are smaller scale structures associated with the convection, and they are displayed in figure 3.1 for various Rayleigh numbers. These figures display volumetric renderings of the temperature fluctuations. The red (hotter) regions represent columns of rising fluid while the blue (colder) regions represent sinking fluid. Both figures 3.1 (a) and (b) show that these structures are tilted along the direction of the magnetic field for large values of the Chandrasekhar number. This is true of other fluid structures as well, such as the mean flow. Additionally, figures 3.1 (a) and (b) show that as the Rayleigh number is increased, the rising and sinking columns of fluid become thinner. For Rayleigh numbers up to approximately $Ra \simeq 3Ra_c$, the convective cells are thicker and the Lorentz force remains a dominant term in the force balance. This region of parameter space will be referred to as the cellular regime. The convective cells for Rayleigh numbers larger than $3Ra_c$ tend to be thinner, and this regime will be referred to as the columnar regime. The temperature fluctuations shown in figure 3.1 (c) correspond to the turbulent regime. Flow regimes similar to the cellular, columnar, and turbulent regimes are observed for convection in vertical magnetic fields [4].

3.3 Mean flow character

3.3.1 Mean flow formation

The flow patterns for Rayleigh numbers just slightly larger than the critical Rayleigh number are similar to those at the onset of convection. This flow structure is shown in figure 3.2 where the Rayleigh number is $Ra = 1.012Ra_c$ and the Chandrasekhar number is $Q = 2 \times 10^6$. Figure 3.2 (a) shows the z-component of velocity in the xy-plane and the rolls from the onset of convection are clearly still intact although there is a large scale modulation running across them. This modulation is related to the formation of a mean flow shown in figure 3.2 (b). The vertical structure of the rolls ceases to be invariant along the z-direction as shown in figures 3.2 (c) and (d). The Fourier spectra are shown in figure 3.3 (a) for the z-component of velocity along the y-direction. The first

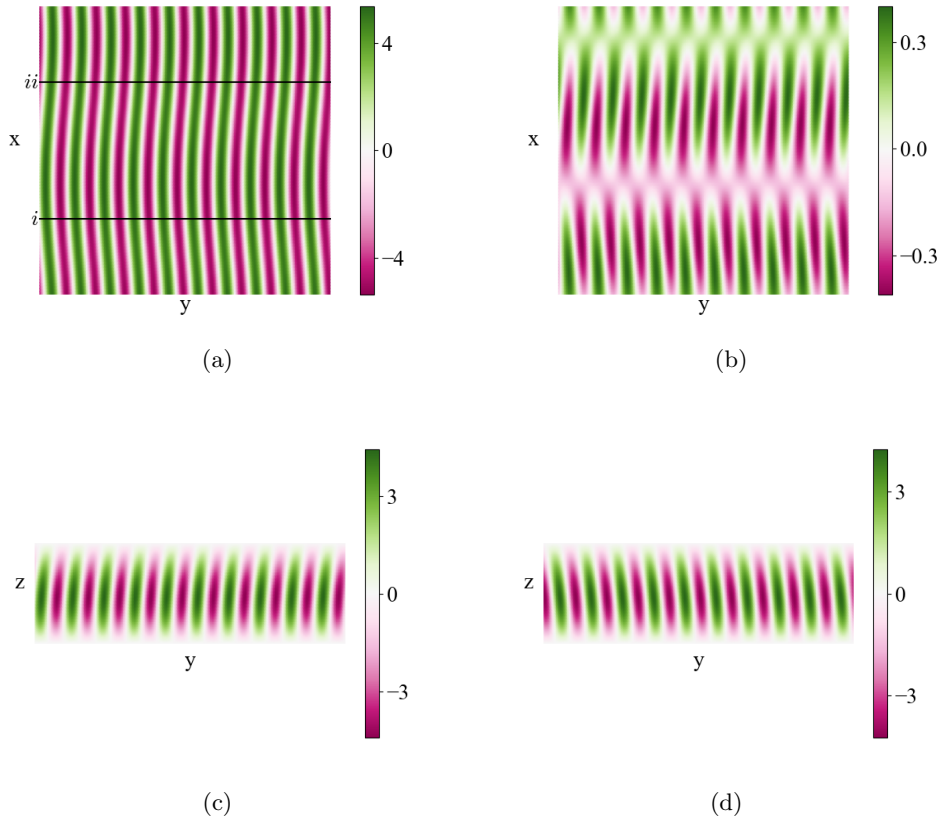

Figure 3.2: Graphs of velocities for the simulation $Q = 2 \times 10^6$, $Ra = 1.04 \times 10^7 = 1.012Ra_c$. (a) The z-component of velocity plotted in the xy-plane in the midplane. (b) The y-component of velocity plotted in the xy-plane in the midplane. (c) The z-component of velocity plotted in the yz-plane at the line i in 3.2 (a). (d) The z-component of velocity plotted in the yz-plane at the line ii in 3.2 (a).

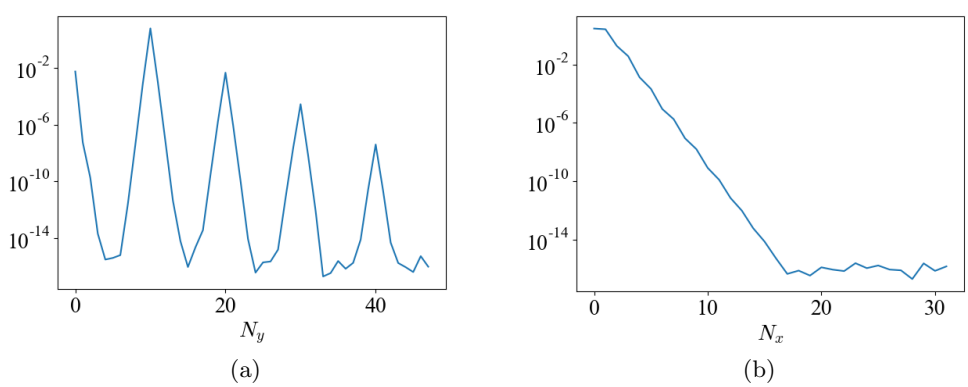

Figure 3.3: Graphs of the Fourier spectra of the z-component of velocity in the midplane for the case $Q = 2 \times 10^6$, $Ra = 1.04 \times 10^7 = 1.012Ra_c$. (a) The spectra along the y-direction. (b) The spectra along the x-direction.

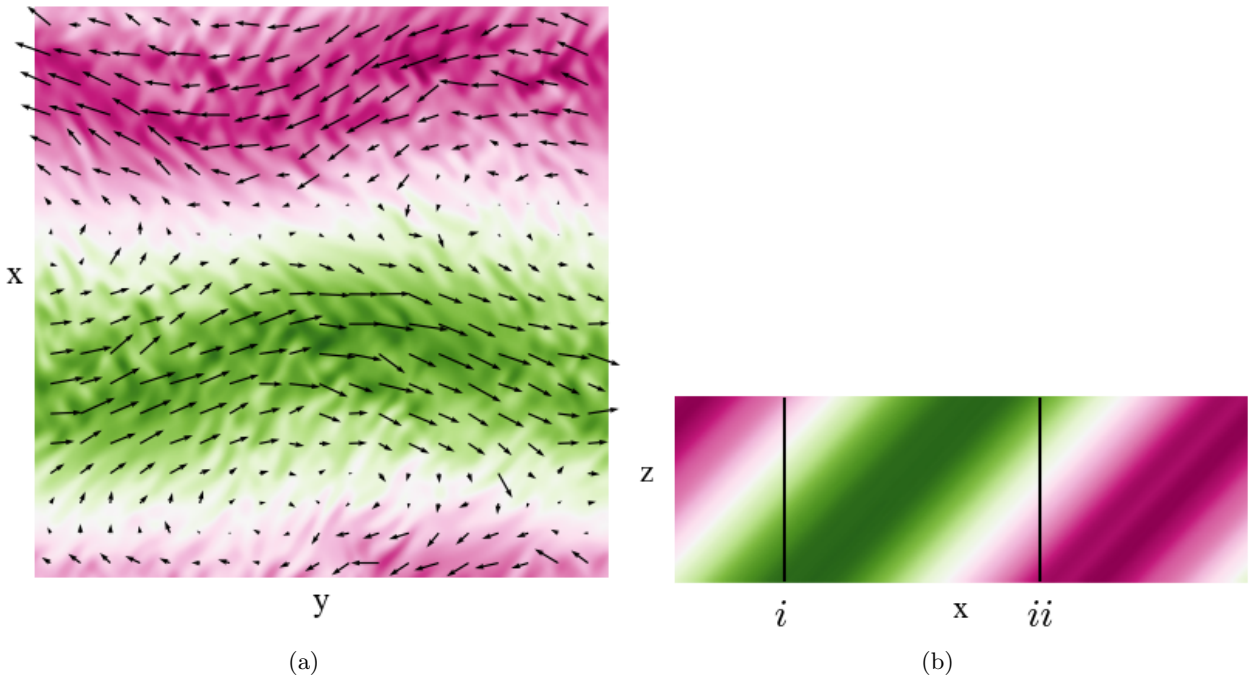

Figure 3.4: Structure of the large scale flow for $Q = 2 \times 10^6$, $Ra = 5 \times 10^7$. Colors represent the y-component of the velocity. (a) A slice of the xy-plane in the midplane where the arrows give the horizontal component of velocity. (b) y-velocity averaged along the y-direction.

and largest spike in frequency space occurs at a frequency of ten and corresponds to the presence of ten rolls in the simulation domain. There are smaller spikes at every tenth frequency in spectral space which is characteristic of a solution interacting with itself via nonlinear terms in an equation.

3.3.2 Characteristics of the mean flow

The mean flow creates a large scale structure that persists for a wide range of Rayleigh numbers. The mean flow is characterized by a y-component of velocity that is mostly constant along the y-direction and has wavenumber one along the x-direction as shown in figure 3.4 (a). The structure of the y-component of velocity does not change much in time for flows not undergoing relaxation oscillations. There is also an x-component of the velocity that acts to form two vortices of opposite vorticity in the xy-plane, which can also be seen in figure 3.4 (a). Unlike the y-component of velocity, the structure of the x-velocity is not constant in time and neither are the vortices. The mean flow is not depth invariant for $Q = 2 \times 10^5$ or $Q = 2 \times 10^6$ but rather follows the

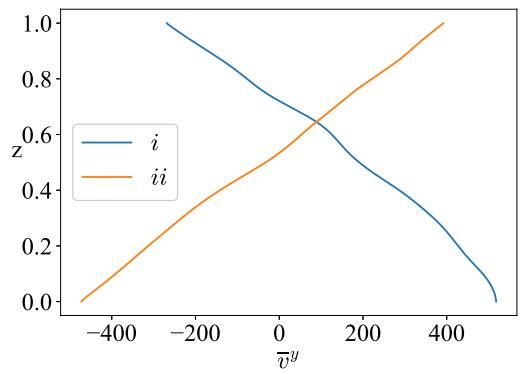

(a)

Figure 3.5: Profiles of the y-velocity averaged along the y-direction corresponding to the lines on figure 3.4 (b).

imposed magnetic field as shown in figure 3.4 (b). This tilting of the mean flow along the magnetic field is more prominent for larger values of the Chandrasekhar number. Figure 3.4 (b) shows that the strength of the mean flow is approximately invariant along the imposed magnetic field. One-dimensional profiles of figure 3.4 (b) are plotted in figure 3.5 for various locations corresponding to the lines on figure 3.4 (b). The profiles are approximately linear and do not display obvious boundary layers. The reason the y-velocity lacks obvious boundary layers may be due to the boundary conditions involving derivatives of the y-velocity, but not the y-velocity itself.

3.3.3 Mean flow equation

The mean flow can be analyzed by averaging the Navier-Stokes equation along the y-direction. Let the notation for an average along the y-direction be given by

$$\overline{f}^y = \frac{1}{L_y}\int_0^{L_y} f dy, \tag{3.1}$$

and the fluctuation along this direction be given by $f' = f - \overline{f}^y$. Averaging the y-component of the Navier-Stokes equation along the y-direction yields

$$\frac{\partial \overline{v}^y}{\partial t} + \overline{\mathbf{u}}^y \cdot \nabla \overline{v}^y + \frac{\partial}{\partial x}\overline{(v'u')}^y + \frac{\partial}{\partial z}\overline{(v'w')}^y = Q\left(\cos\theta\frac{\partial}{\partial z} + \sin\theta\frac{\partial}{\partial x}\right)\overline{b}_y^y + \nabla_\perp^2 \overline{v}^y, \tag{3.2}$$

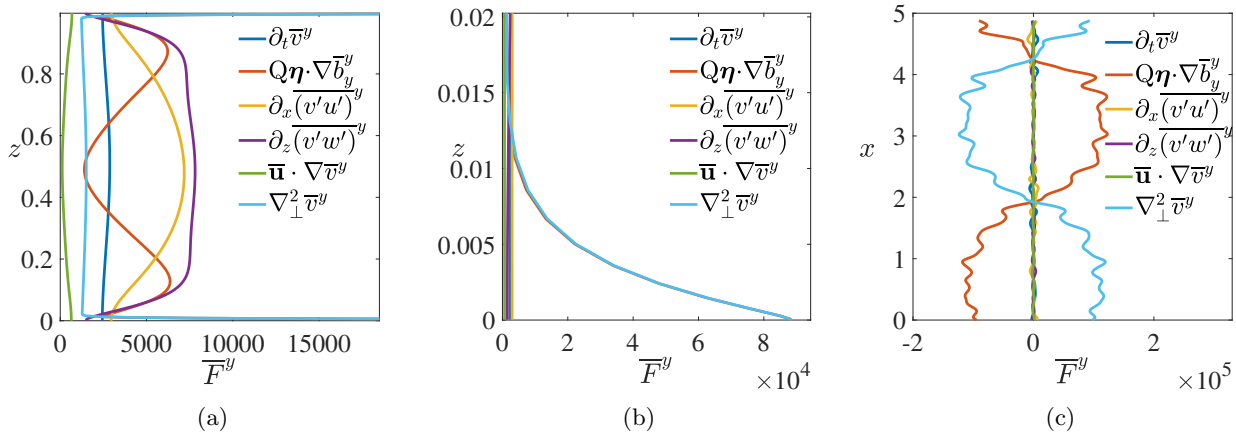

Figure 3.6: Plots of all terms given in equation 3.2 at one instant in time for $Q = 2 \times 10^5$, $Ra = 6 \times 10^6$. (a) Plot of rms values for the entire simulation domain. (b) Plot of rms values within the boundary layer. Note that the magnetic and viscous terms overlie one another. (c) Slice of data in the boundary layer as a function of x.

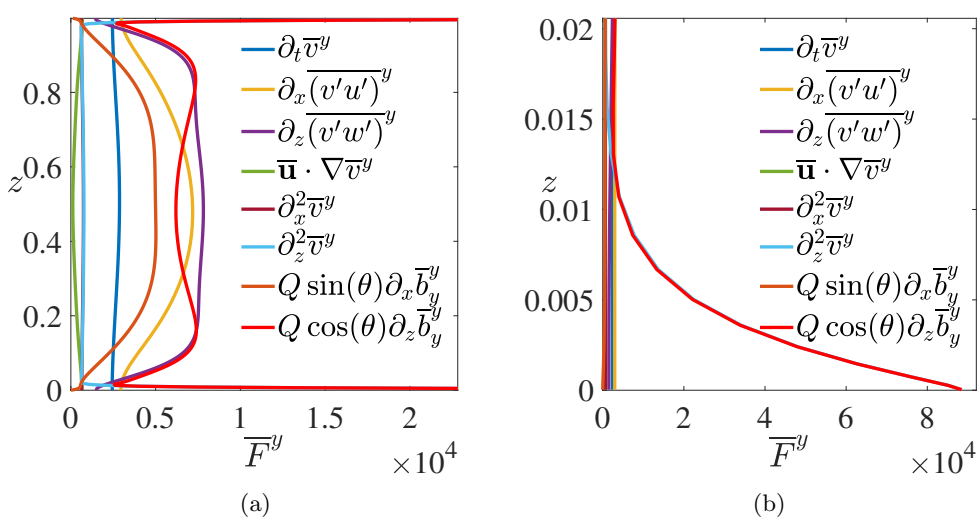

Figure 3.7: Plots of rms values of all the terms given in equation 3.2 at one instant in time for $Q = 2 \times 10^5$, $Ra = 6 \times 10^6$ with the magnetic and viscous terms further split up. (a) The entire simulation domain. (b) The boundary layer. Note that the terms $\partial_z^2\overline{v}^y$ and $Q\cos(\theta)\partial_z\overline{b}_y^y$ overlie one another in the boundary layer.

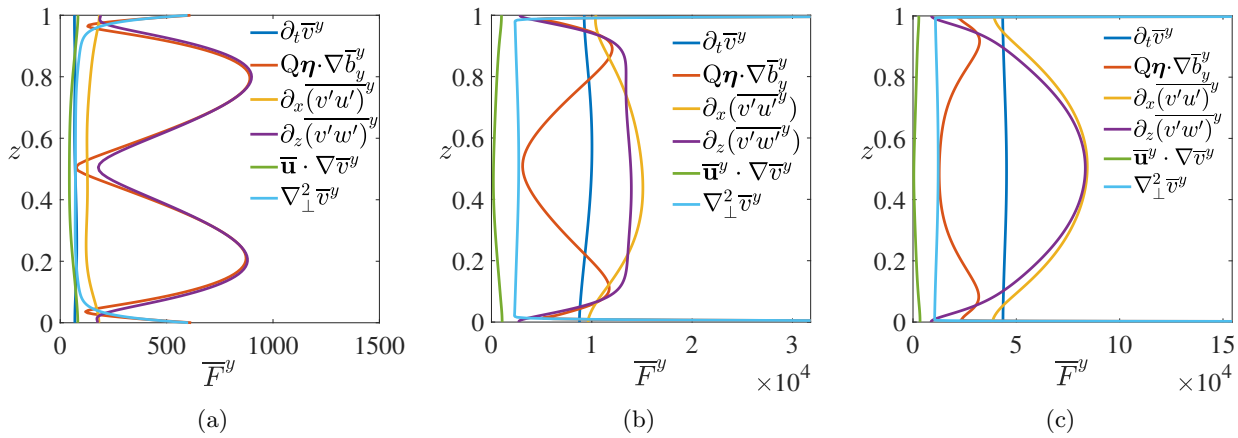

Figure 3.8: Plots of rms values of all the terms given in equation 3.2 at one instant in time for different values of Q. (a) $Q = 2 \times 10^3$, $Ra = 6.58Ra_c$. (b) $Q = 2 \times 10^5$, $Ra = 7.42Ra_c$. (c) $Q = 2 \times 10^6$, $Ra = 6.81Ra_c$.

where $\nabla_\perp^2 = \frac{\partial^2}{\partial x^2} + \frac{\partial^2}{\partial z^2}$. The two terms $\overline{(v'u')}^y$ and $\overline{(v'w')}^y$ are the Reynolds stresses. Reynolds stresses physically represent the flux of momentum in a given direction. The two Reynolds stresses presented are the flux of y-momentum in the x-direction, and the flux of y-momentum in the z-direction, respectively.

Figures 3.6 (a) and (b) display an rms at one instant in time of the different terms in equation 3.2 for the columnar regime with $Q = 2 \times 10^5$, $Ra = 6 \times 10^6$. The rms is performed along the x-direction. Near the midplane of the simulation domain, the Reynolds terms are the largest terms. The only term in the equation that is negligible over the entire simulation domain is $\overline{\mathbf{u}}^y \cdot \nabla\overline{v}^y$. Boundary layers are observed, where the viscous and magnetic forces become large and approximately balance one another. Figure 3.6 (c) shows an x-slice of the boundary layer where it can be seen that the viscous and magnetic forces undergo one complete oscillation over the length of the simulation domain along the x-direction. This suggests the mean flow may be responsible for this boundary layer because the mean flow similarly has wavenumber one along the x-direction.

The terms in equation 3.2 can be broken apart further. In particular, the magnetic and viscous forces can be split into parts consisting of either x or z derivatives. This gives

$$\nabla_\perp^2 \overline{v}^y = \frac{\partial^2 \overline{v}^y}{\partial x^2} + \frac{\partial^2 \overline{v}^y}{\partial z^2}, \tag{3.3}$$

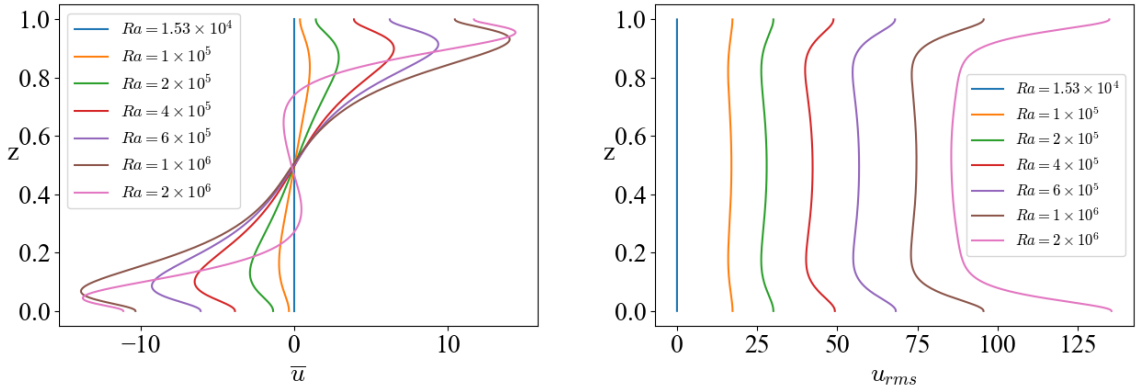

(a) (b)

Figure 3.9: The x-component of velocity averaged in time as a function of vertical height for selected cases from $Q = 2 \times 10^3$. (a) Horizontal average. (b) Horizontal rms.

and

$$Q\boldsymbol{\eta} \cdot \nabla \overline{b}_y^y = Q \cos\theta \frac{\partial \overline{b}_y^y}{\partial z} + Q \sin\theta \frac{\partial \overline{b}_y^y}{\partial x}. \tag{3.4}$$

Of particular interest is determining which parts of the viscous and magnetic forces become large in the boundary layer. Equation 3.2 is graphed with the viscous and magnetic terms further broken up in figure 3.7, from which the boundary layer balance becomes

$$Q \cos\theta \frac{\partial \overline{b}_y^y}{\partial z} + \frac{\partial^2 \overline{v}^y}{\partial z^2} \simeq 0. \tag{3.5}$$

Additionally, it is interesting to analyze how the forces associated with the mean flow change as a function of the Chandrasekhar number. Figure 3.8 shows the forces for the three investigated values of the Chandrasekhar number. For $Q = 2 \times 10^3$, the Reynolds force, $\frac{\partial}{\partial x}\overline{(v'u')}^y$, and the time derivative term are far smaller than they are for the larger values of Q. The Reynolds forces for $Q = 2 \times 10^3$ are small near the midplane but are large in the midplane for the Chandrasekhar numbers $Q = 2 \times 10^5$ and $Q = 2 \times 10^6$. Also, the boundary layer thickness decreases as Q is increased.

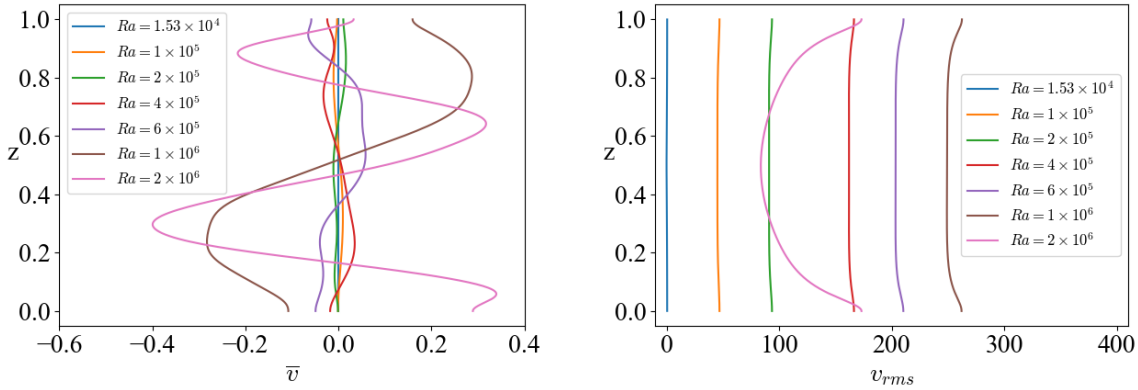

(a) (b)

Figure 3.10: The y-component of velocity averaged in time as a function of vertical height for selected cases from $Q = 2 \times 10^3$. (a) Horizontal average. (b) Horizontal rms.

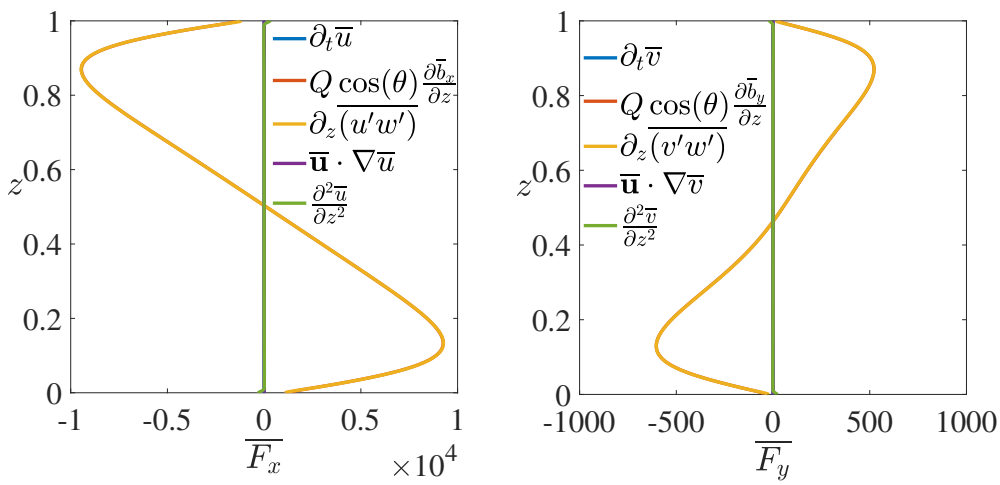

(a) (b)

Figure 3.11: Plots of the terms in equation 3.7 at one instant in time for $Q = 2 \times 10^5$, $Ra = 6 \times 10^6$. Note that the magnetic term and the Reynolds term overlie one another. (a) The x-component terms. (b) The y-component terms.

3.3.4 Horizontally averaged velocities and forces

The dependence of the x-component of velocity on z can be studied by taking a horizontal average and a horizontal rms of the x-velocity, where a horizontal rms of a velocity is defined as

$$u_{rms} = \left(\frac{1}{L_x L_y} \int_0^{L_x} \int_0^{L_y} (u - \overline{u})^2 dy dx \right)^{\frac{1}{2}}. \tag{3.6}$$

Figure 3.9 (a) shows the horizontally averaged x-component of velocity as a function of vertical height. This averaged x-velocity is positive near the top of the simulation domain and negative near the bottom of the simulation domain. This overturning motion was also observed in a two-dimensional study of convection with a tilted magnetic field [6]. However, the rms x-velocity shown in figure 3.9 (b) is over five times as large as the averaged x-velocity. This suggests that while the averaged x-velocity has a distinct nonzero profile, it is not a dominant factor in the dynamics of the simulations. This is true for higher values of the Chandrasekhar number as well.

Figure 3.10 shows the same plots for the y-component of velocity. There is not a simple profile for the horizontally averaged y-component of velocity as there was for the x-component of velocity. The averaged y-velocity is more than two orders of magnitude smaller than the rms y-velocity, so the horizontally averaged y-velocity is negligible to the dynamics. From figure 3.10 (b), it can also be seen that the y-component of velocity changes greatly in the turbulent regime ($Ra = 2 \times 10^6$) where the rms y-velocity decreases below simulations with a smaller Rayleigh number. The rms y-velocity for the turbulent regime also ceases to be mostly depth invariant and is instead larger near the boundaries.

Taking the horizontal average of the x-component and y-component of the Navier-Stokes equation yields

$$\frac{\partial \overline{u}}{\partial t} + \overline{\mathbf{u}} \cdot \nabla \overline{u} + \frac{\partial}{\partial z}\overline{(u'w')} = Q \cos\theta \frac{\partial \overline{b}_x}{\partial z} + \frac{\partial^2 \overline{u}}{\partial z^2}, \qquad \frac{\partial \overline{v}}{\partial t} + \overline{\mathbf{u}} \cdot \nabla \overline{v} + \frac{\partial}{\partial z}\overline{(v'w')} = Q \cos\theta \frac{\partial \overline{b}_y}{\partial z} + \frac{\partial^2 \overline{v}}{\partial z^2}, \quad (3.7)$$

respectively. The terms for these equations are shown in figure 3.11 at one instant in time for $Q = 2 \times 10^5$, $Ra = 6 \times 10^6$. Note that the y-component terms are approximately an order of magnitude smaller than the x-component terms, which is to be expected since the horizontally averaged x-component of velocity is over an order of magnitude larger than the horizontally averaged y-component of velocity.

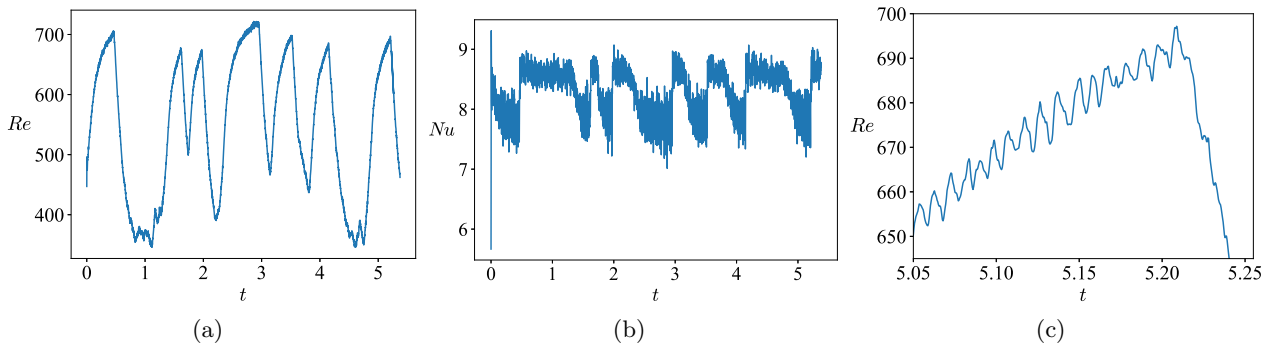

Figure 3.12: Reynolds and Nusselt number plots for $Q = 2 \times 10^5$, $Ra = 1.5 \times 10^7$. (a) Plot showing the time evolution of the Reynolds number. (b) Plot showing the time evolution of the Nusselt number. (c) Close up of Reynolds number graph at a peak.

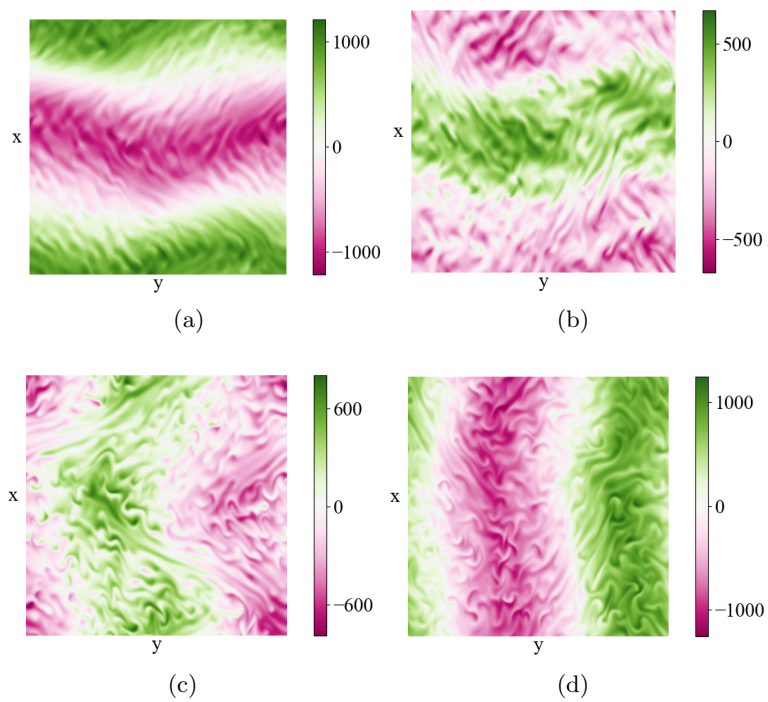

Figure 3.13: Plots of an xy-slice of velocity data for $Q = 2 \times 10^5$, $Ra = 1.5 \times 10^7$ at different times. The left figures are made at a time just before the Reynolds number reaches a peak ($t = 5.200$) and the graphs at the right just after the Reynolds number peaks ($t = 5.228$). (a) & (b) The y-component of velocity. (c) & (d) The x-component of velocity.

3.3.5 Relaxation oscillations

Relaxation oscillations occur for $Q = 2 \times 10^5$ and $10Ra_c \lesssim Ra \leq 30Ra_c$, where $30Ra_c$ was the highest Rayleigh number achieved for this Chandrasekhar number. The relaxation oscillations

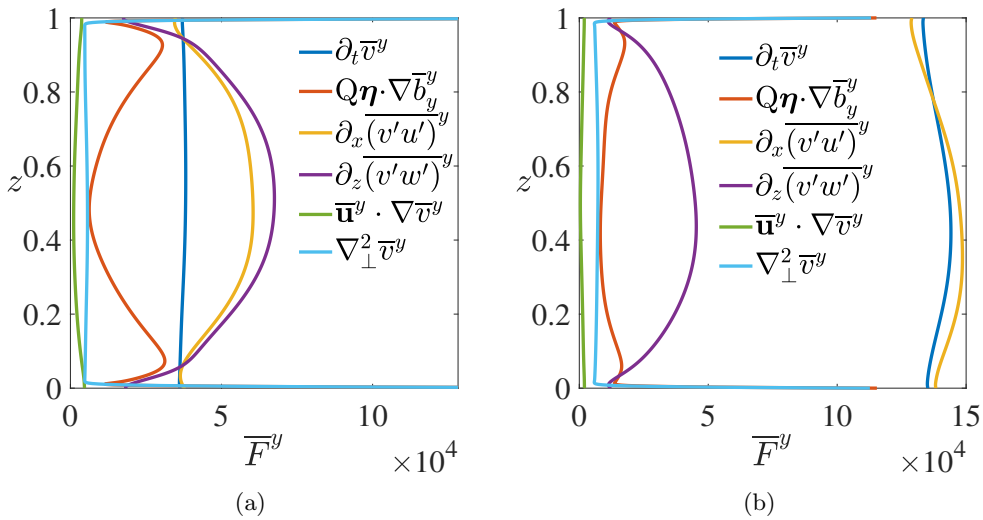

Figure 3.14: Plots of the terms in equation 3.2 for $Q = 2 \times 10^5$, $Ra = 1.5 \times 10^7$ at two times. (a) The terms just before the Reynolds number peaks ($t = 5.200$). (b) The terms just after the Reynolds number peaks ($t = 5.228$).

consist of the mean flow strength growing and shrinking over time, giving rise to large changes in the Reynolds number and Nusselt number. These changes in time are shown in figure 3.12. The mean flow peaks in strength near the regions just before the Reynolds number peaks, and the Nusselt number is smaller in these regions. This behavior indicates an inverse relationship between the mean flow and heat transport. Figure 3.13 shows how the horizontal components of velocity change when the Reynolds number goes from increasing to decreasing. The y-component of the velocity decays rapidly and the x-component of velocity grows to be the dominant velocity component. Based on figure 3.12 (a), the total speed of the fluid then decreases for some time after the x-component of velocity becomes the dominant component.

The method of using averages along the y-direction introduced in the mean flow section can be used to better understand what causes the mean flow to weaken. By determining how the terms of equation 3.2 change in time, the forces responsible for the changes in the mean flow can be identified. This is shown in figure 3.14. Before the mean flow starts to diminish, the forces are similar to those of $Q = 2 \times 10^5$, $Ra = 6 \times 10^6$ for a steady mean flow. After the Reynolds number peaks and the mean flow starts to weaken, the forces change drastically. As shown in figure 3.14

(b), the term $\partial_t \overline{v}^y$ grows large and represents the weakening of the y-component of velocity. The time derivative of the y-velocity is balanced by the Reynolds force $\frac{\partial}{\partial x}\left(\overline{v'u'}\right)$, which represents the flux of y-momentum caused the x-component of velocity carrying fluid from the region with positive (negative) y-velocity to the region with negative (positive) y-velocity.

The inverse relation between the mean flow strength and heat transport shown in figure 3.12 may indicate that the mean flow restricts the convection. This suggests that, as the mean flow grows in strength, it cuts off the convection that supplies energy to it. The contribution of the convection to the mean flow is encompassed in the term $\frac{\partial}{\partial z}\left(\overline{v'w'}\right)$, which decreases after the Reynolds number peaks, and this decrease supports the claim that the mean flow undergoes relaxation oscillations due to the mean flow restricting convection.

3.4 Balances in the governing equations

Balances provide a way of determining which terms in an equation are dominant and how the terms change for different flow regimes. Figure 3.15 displays the instantaneous horizontal rms of the z-component of the forces in the Navier-Stokes equation for three flow regimes. For the balances, the horizontal rms is defined as

$$\left(\frac{1}{L_x L_y}\int_0^{L_x}\int_0^{L_y} F^2 dydx\right)^{\frac{1}{2}}. \tag{3.8}$$

For the cellular regime, the buoyancy force and the Lorentz force are the dominant vertical forces near the midplane of the fluid with pressure playing a smaller role and the rest being negligible. In the cellular and columnar regimes, there exists an approximate balance of the pressure and Lorentz forces in the boundary layer, which can be seen in figures 3.15 (a) and (b). For the columnar regime, the advection term and the time rate change of velocity are the largest terms in the midplane. This is due to the presence of the mean flow. The mean flow has a tendency to move the rising columns of fluid with it, leading to a large partial time derivative. The time derivative term is in part balanced by the advection term, with the sum of these two terms being much smaller than either individually. Figure 3.15 (c) shows the turbulent regime, and from this figure it can be seen that

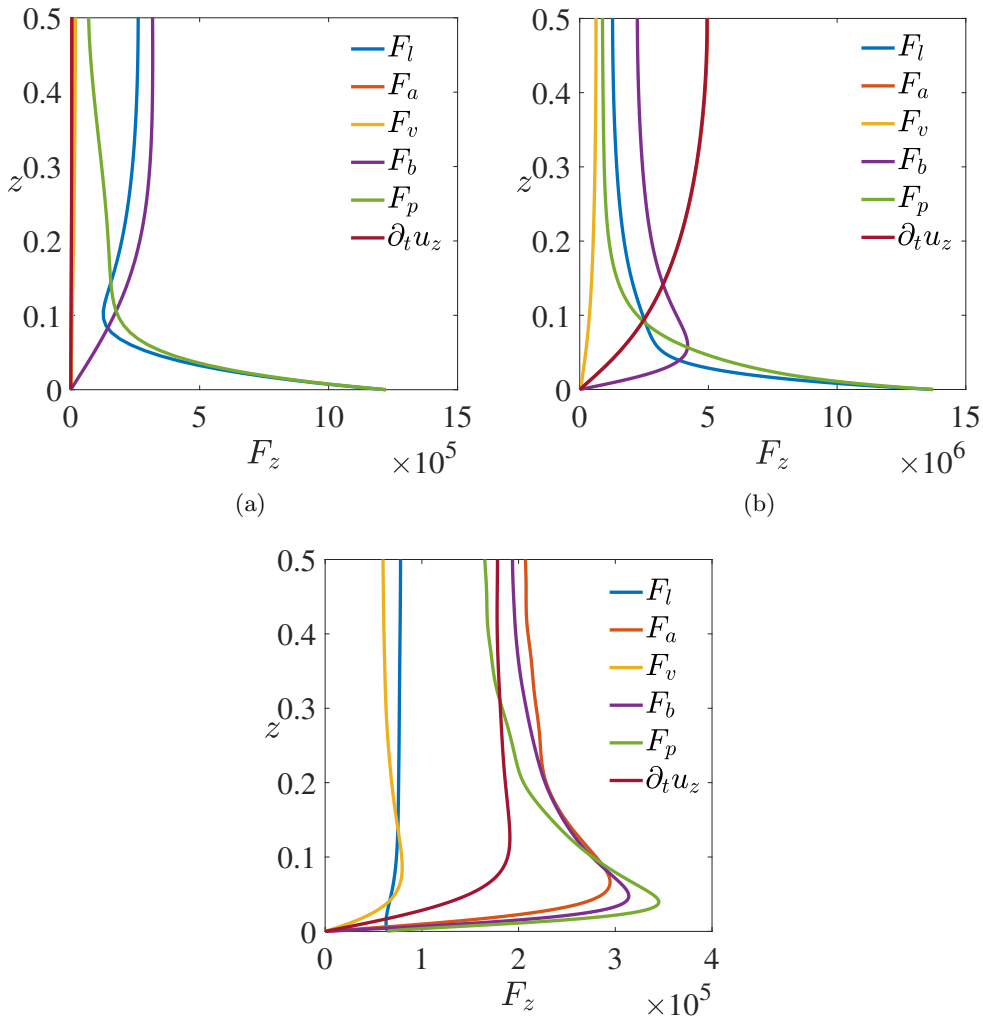

Figure 3.15: Plots showing a horizontal rms of the vertical forces from the Navier-Stokes equation at one instant in time for different flow regimes. (a) The cellular regime with $Q = 2 \times 10^6$, $Ra = 1.3 \times 10^7$. (b) The columnar regime with $Q = 2 \times 10^6$, $Ra = 7 \times 10^7$. (c) The turbulent regime with $Q = 2 \times 10^3$, $Ra = 2 \times 10^6$.

the time derivative term and the advection term are no longer the two largest terms. This is due to the mean flow having dissipated. Additionally, the Lorentz force is playing a much smaller role in the dynamics, but is still larger than the viscous force over the majority of the simulation domain. Thus the magnetic field continues to be a non-negligible term for Rayleigh numbers up to at least $Ra = 100Ra_c$ for $Q = 2 \times 10^3$.

Figure 3.16 displays the instantaneous horizontal rms of the horizontal component of the

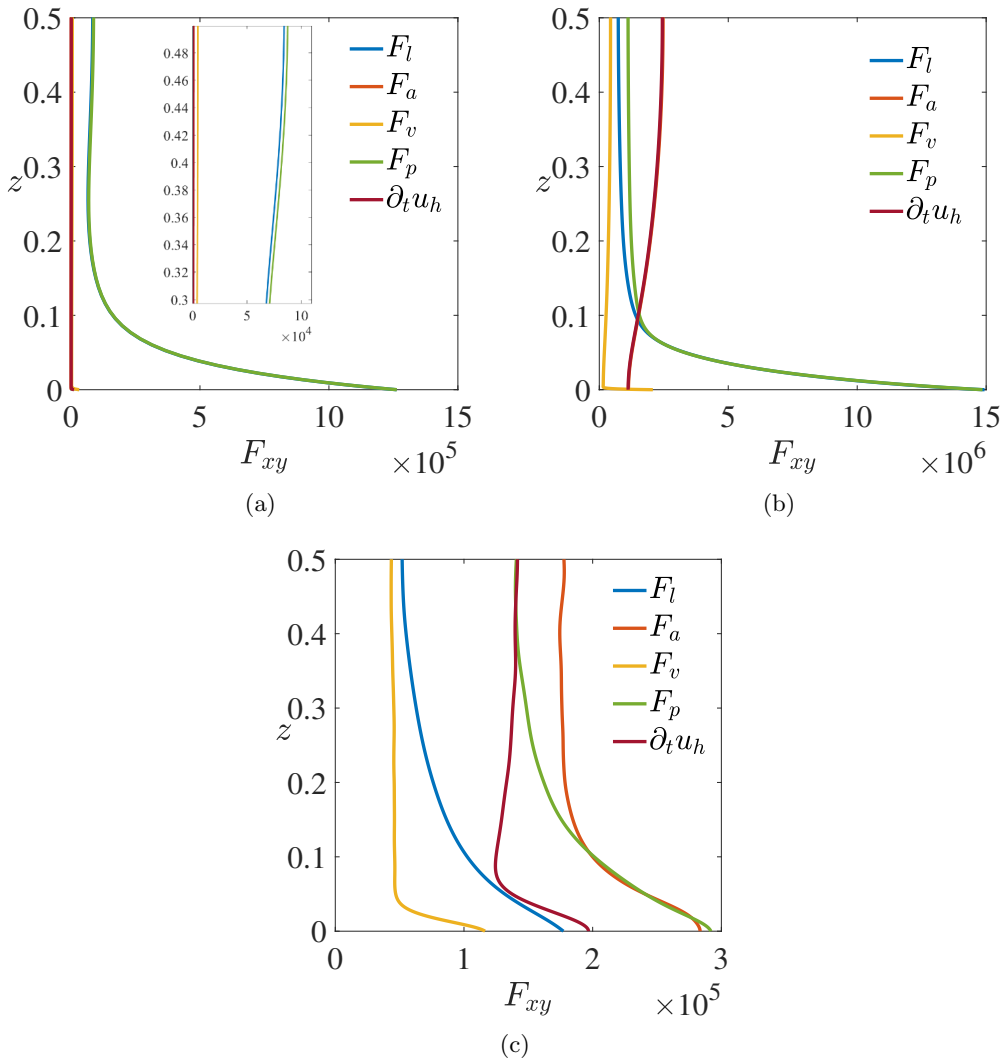

Figure 3.16: Plots showing a horizontal rms of the horizontal forces from the Navier-Stokes equation at one instant in time for different flow regimes. u_h is the horizontal component of velocity. (a) The cellular regime with $Q = 2 \times 10^6$, $Ra = 1.3 \times 10^7$ along with a zoom in of the upper left corner. (b) The columnar regime with $Q = 2 \times 10^6$, $Ra = 7 \times 10^7$. (c) The turbulent regime with $Q = 2 \times 10^3$, $Ra = 2 \times 10^6$.

forces in the Navier-Stokes equation for three flow regimes. Note that $u_h = (u, v, 0)$. The horizontal rms of a horizontal force is given by

$$\left(\frac{1}{L_x L_y} \int_0^{L_x} \int_0^{L_y} \left(F_x^2 + F_y^2 \right) dy dx \right)^{\frac{1}{2}} \tag{3.9}$$

where F_x is the x-component of a term in the Navier-Stokes equation and F_y is the y-component of a term in the Navier-Stokes equation. Figure 3.16 (a) shows that in the cellular regime, the dominant

forces are the Lorentz force and the pressure force throughout the entire simulation domain. Even in the midplane of the simulation domain where the Lorentz and pressure forces are smaller, both of these terms are over an order of magnitude larger than the rest of the terms. In the columnar and cellular regimes, the Lorentz and pressure terms are the leading-order terms in the boundary layer. In the columnar regime, the mean flow once again causes the partial derivative of velocity with respect to time to be an important term and again the advection term acts to balance this. The viscous force in the columnar regime has a thin boundary layer corresponding to the same boundary layer seen in figure 3.6. Figure 3.15 (b) is the only simulation shown in figure 3.15 with a strong mean flow, and suggests the mean flow is responsible for this boundary layer.

Figure 3.17 displays instantaneous horizontal rms of the temperature terms for the cellular, columnar, and turbulent regime. Note that

$$u_h \cdot \nabla_h T' = u\frac{\partial T'}{\partial x} + v\frac{\partial T'}{\partial y}, \qquad \nabla_h^2 T' = \frac{\partial^2 T'}{\partial x^2} + \frac{\partial^2 T'}{\partial y^2}. \tag{3.10}$$

In the columnar regime, the mean flow moves columns of convecting fluid which carry large temperature fluctuations; this leads to the term $\partial_t T'$ being large. This is partially balanced by the term $u_h \cdot \nabla_h T'$. Once again, in the turbulent regime these terms are no longer dominant since the mean flow has decayed. In the turbulent regime, the two terms $w\partial_z \overline{T}$ and $\partial_z \left(\overline{wT}\right)$ become negligible in the midplane of the simulation domain.

3.5 Influence of the aspect ratio

Also of interest is how the various aspects of the flow depend on the aspect ratio. The mean flow is observed to adapt its size to fit the entire simulation domain. The flow speeds depend on the aspect ratio which can be seen in figure 3.18 (a). In particular, the Reynolds number scales nearly linearly with the aspect ratio for $\Gamma \gtrsim 10\lambda_c$. This relation is due to the fact that the energy entering the system is proportional to the cross-sectional area of the domain. Then, if the mean flow strength is proportional to the energy entering the system, the Reynolds number scales linearly with aspect ratio. The reason that this linear relationship fails for $\Gamma = 7\lambda_c$ is that the strength of

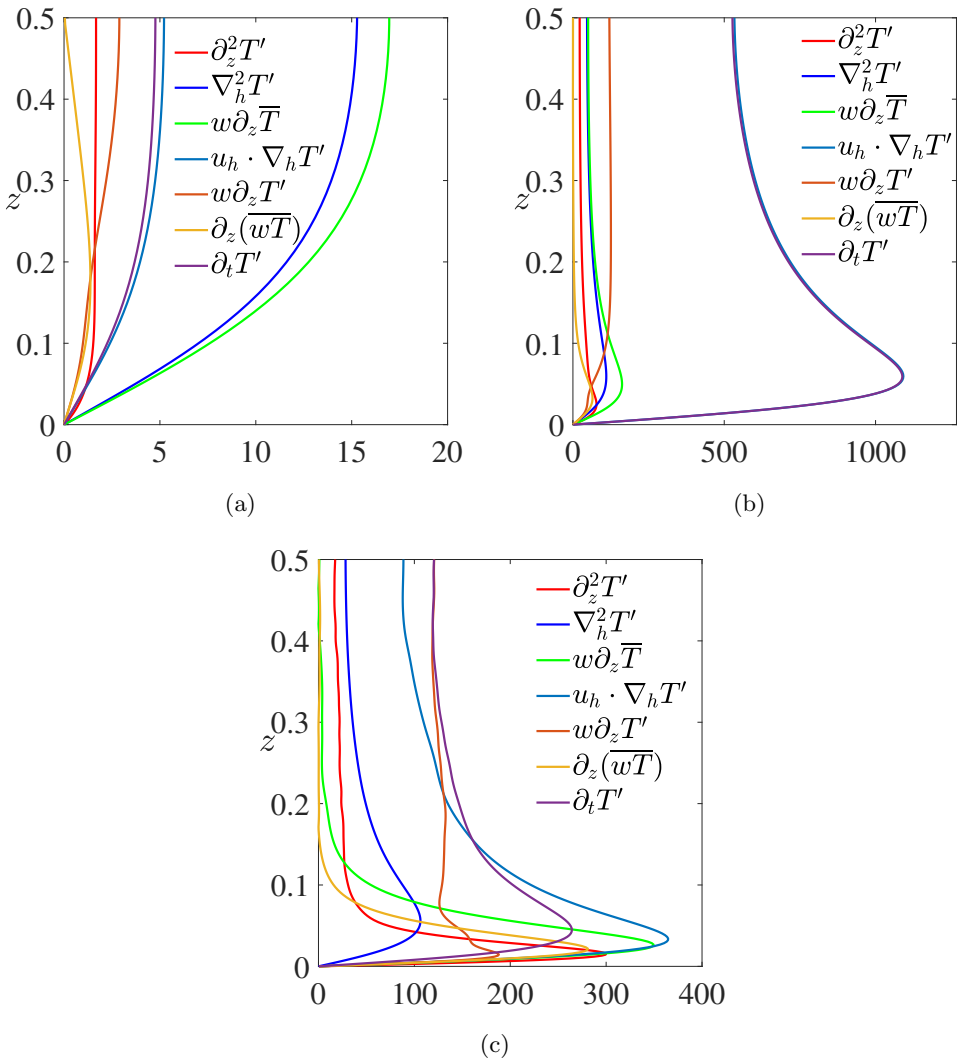

Figure 3.17: Plots showing a horizontal rms of temperature terms at one instant in time for different flow regimes. u_h is the horizontal component of velocity. (a) The cellular regime with $Q = 2 \times 10^6$, $Ra = 1.3 \times 10^7$. (b) The columnar regime with $Q = 2 \times 10^6$, $Ra = 7 \times 10^7$. (c) The turbulent regime with $Q = 2 \times 10^3$, $Ra = 2 \times 10^6$.

the mean flow ceases to remain constant in time for smaller aspect ratios.

It is useful to define the convective Reynolds number as

$$Re_z = \langle w^2 \rangle^{\frac{1}{2}}. \tag{3.11}$$

Figure 3.18 (b) displays Re_z for several aspect ratios and shows that Re_z is fairly constant for aspect ratios $\Gamma \gtrsim 10\lambda_c$. The Nusselt number does not vary much with Γ either, which is to be

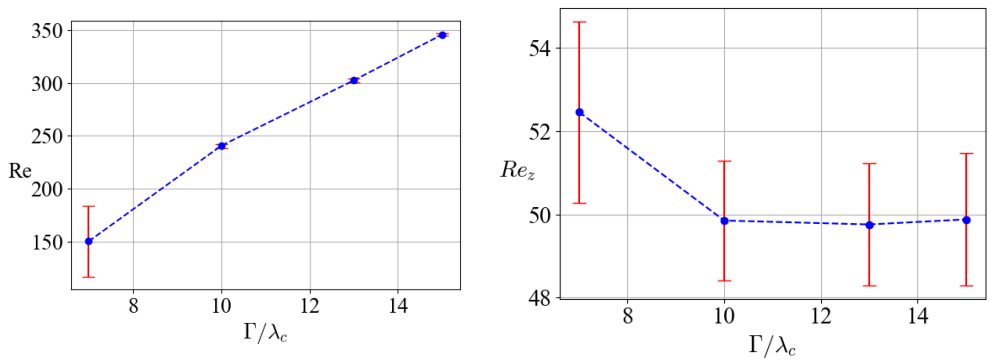

(a) (b)

Figure 3.18: Plots of $Q = 2 \times 10^5$ and $Ra = 6 \times 10^6$ for different aspect ratios where the bars represent the standard deviation in time. (a) The Reynolds number. (b) The convective Reynolds number.

expected since the Nusselt number measures the flow of heat which is strongly correlated with the z-velocity of the fluid. Because Re_z does not vary much with the aspect ratio, it is useful for comparing flow speeds in a way independent of the size of the simulation domain.

3.6 Reynolds number scaling

The mean flow gives rise to large velocities in the y-direction that are a determining factor in the Reynolds number. These large y-velocities can be seen in figure 3.19, where v^2 is the largest component of velocity squared for a wide range of Rayleigh numbers. Since the density of the fluid is assumed constant under the Boussinesq approximation, the kinetic energy of the fluid is proportional to the square of the velocity, so figure 3.19 (a) also gives the ratios of the kinetic energy from each component of velocity. The mean flow persists until roughly $100Ra_c$ for $Q = 2 \times 10^3$, after which the mean flow disappears. This causes the y-component of velocity to decrease, which leads to the z-component of velocity becoming the largest velocity component.

The Reynolds number, displayed in figure 3.20 (a), shows that the Reynolds number increases with increasing Rayleigh number. The two exceptions to Re increasing with Ra are the dissipation of the mean flow for $Q = 2 \times 10^3$, $Ra \sim 100Ra_c$, and the start of the relaxation oscillations for $Q = 2 \times 10^5$, $Ra \sim 10Ra_c$. The Reynolds number grows more rapidly with Ra/Ra_c for larger

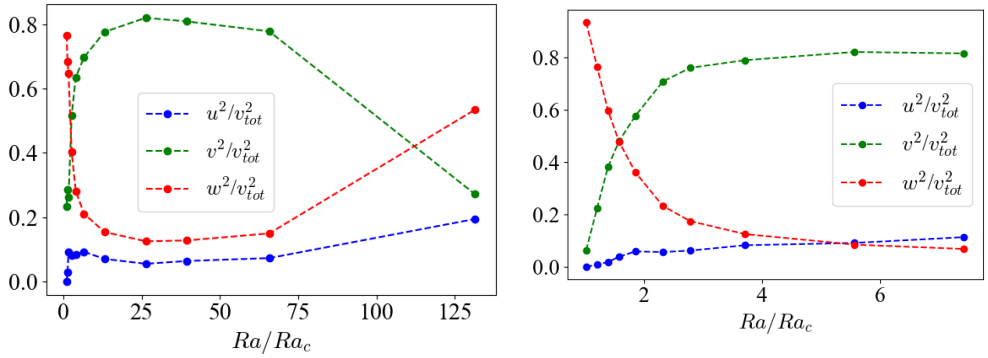

(a) (b)

Figure 3.19: Kinetic energy ratios from the three velocity components averaged in time. (a) Kinetic energy ratios for $Q = 2 \times 10^3$. (b) Kinetic energy ratios for $Q = 2 \times 10^5$.

values of Q. The convective Reynolds number is shown in figure 3.20 (b). The convective Reynolds number tends to be much smaller than the Reynolds number due to the mean flow. Note that no obvious power law scaling exists of the form $Re \sim Ra^a$ or $Re_z \sim Ra^a$. However, for convection with a vertical magnetic field, a power law scaling of the form $Re \sim Ra^a$ does exist for a range of Rayleigh numbers [4].

3.7 Tilt of convective cells along the magnetic field

As mentioned earlier, the convective cells are tilted along the magnetic field for the cellular and columnar regimes with the effect more pronounced for larger values of the Chandrasekhar number. This effect has been observed in other studies of convection with oblique magnetic fields [6]. Figure 3.21 displays how the velocity in the xz-plane is linked to these convective cells. Rising fluid has a tendency to move rightward and sinking fluid has a tendency to move leftward. This can be made quantitative using correlations. The correlation between two measured quantities, say u and w, is given by

$$[u, w] = \frac{\langle uw \rangle}{\sqrt{\langle u^2 \rangle \langle w^2 \rangle}}. \tag{3.12}$$

This correlation was computed for the simulation $Q = 2 \times 10^5$, $Ra = 6 \times 10^6$ and it was found that $[u, w] = 0.324 \pm 0.060$ and $[w, T'] = 0.707 \pm 0.010$, where the error given is the standard

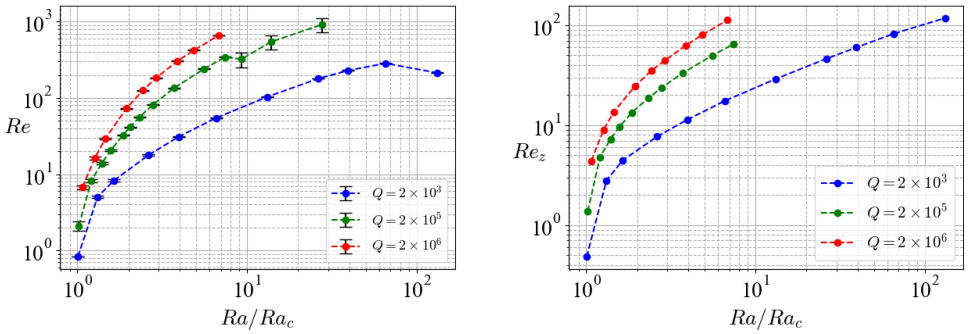

(a) (b)

Figure 3.20: Flow speeds as measured by the Reynolds number. (a) The Reynolds number where bars denote standard deviation in time. (b) The convective Reynolds number.

deviation in time. Thus there exists a large correlation between the temperature fluctuation and the z-component of velocity, as would be expected. The correlation between the z-component of velocity and x-component of velocity is smaller by comparison but is still significant. Moreover, the standard deviation in time for the correlation between u and w is much larger than that between w and T'. The reason for this large standard deviation is that there is a global component to the x-velocity that is not constant in time. This global component of velocity affects the correlations and leads to a large standard deviation in time.

The correlation between u and w for the simulation $Q = 2 \times 10^3$ and $Ra = 1 \times 10^5$ was $[u, w] = .371 \pm .044$, which is higher than the correlation for the simulation $Q = 2 \times 10^5$, $Ra = 6 \times 10^6$. It is slightly odd that a lower Q value would have a larger correlation considering that the magnetic field is the cause of these correlations. One might therefore expect that the case with a larger magnetic field would have a greater correlation. The reason $Q = 2 \times 10^3$ has the larger correlation is again due to the global component of the x-velocity, which grows larger for higher values of the Chandrasekhar number and acts to dampen this correlation.

These claims of the mean flow interfering with the correlation can be verified by subtracting the global component of the x-velocity and using this fluctuating velocity for the correlations. That

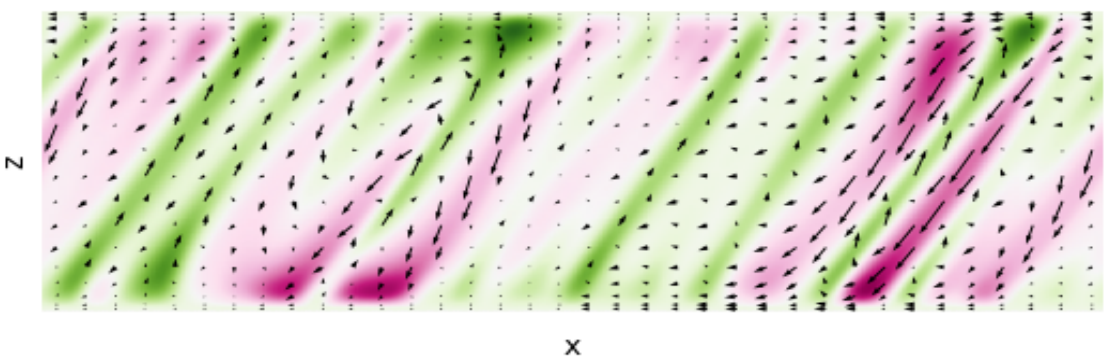

Figure 3.21: Simulation of $Q = 2 \times 10^5$, $Ra = 6 \times 10^6$ with temperature fluctuation plotted as a color; green is positive and pink is negative. The vectors represent the velocity projected into the xz-plane.

is, we define

$$\overline{u}^x = \frac{1}{L_x} \int_0^{L_x} u dx \tag{3.13}$$

and the fluctuating component of x-velocity is then $u' = u - \overline{u}^x$. Using this, the correlation for the case $Q = 2 \times 10^5$, $Ra = 6 \times 10^6$ was calculated to be $[u', w] = 0.474 \pm 0.043$, and for the case $Q = 2 \times 10^3$, $Ra = 10^5$, the correlation was $[u', w] = 0.441 \pm 0.019$. Note that the standard deviation in time of this correlation decreased for both of these cases which suggests the global component of the x-velocity is in fact contributing to the standard deviation in time. The correlation also increased for both of these cases, suggesting that the global component of x-velocity is inhibiting the correlation between the x and z components of velocity. Moreover, the correlation is now slightly larger for the higher Chandrasekhar number case, as might have been expected.

3.8 Heat transport

The Nusselt number measures the heat transport through the system, and is shown in figures 3.22 (a) and (b). Figure 3.22 (a) shows that the Nusselt number increases most rapidly near the onset of convection and increases more slowly for increasing Rayleigh numbers. The slope stays constant longer for higher values of the Chandrasekhar number. In particular, from figure 3.22 (b), the Nusselt number is bounded by the line $y = Ra/Ra_c$ for values of the Chandrasekhar number up to $Q = 2 \times 10^6$. It would be interesting to see if this holds for higher values of the Chandrasekhar

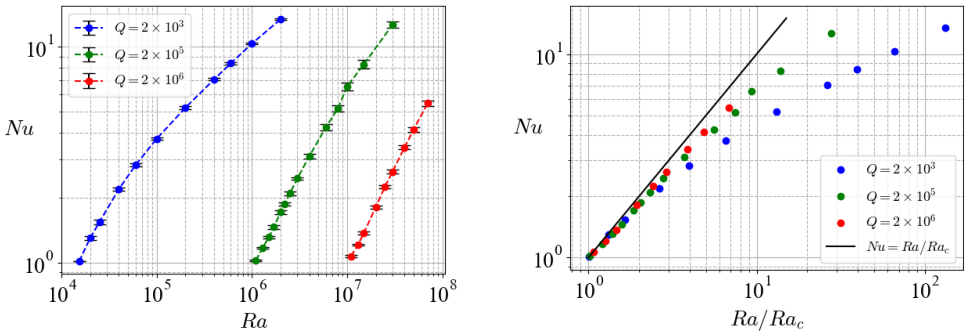

(a) (b)

Figure 3.22: Plots of the Nusselt number for various Rayleigh and Chandrasekhar numbers. (a) The Nusselt number as a function of the Rayleigh number where bars denote standard deviation in time. (b) The Nusselt number as a function of the Rayleigh number normalized by the critical Rayleigh number.

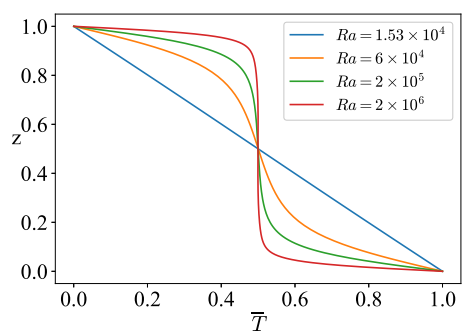

Figure 3.23: The mean temperature $\overline{T}$ as a function of the height of the simulation domain for $Q = 2 \times 10^3$.

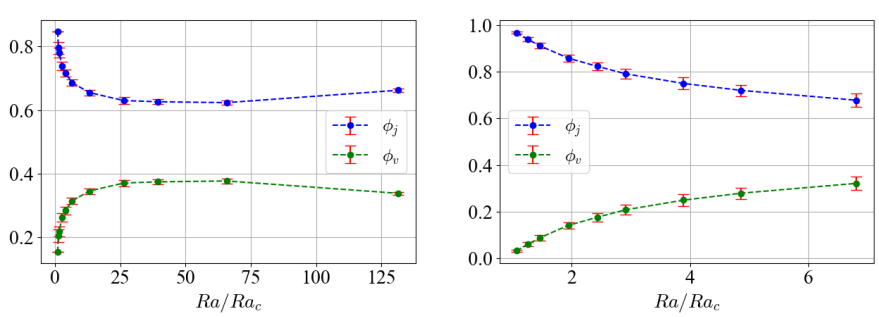

(a) (b)

Figure 3.24: Dissipation ratios where bars denote standard deviation in time for two values of the Chandrasekhar number : (a) $Q = 2 \times 10^3$; (b) $Q = 2 \times 10^6$.

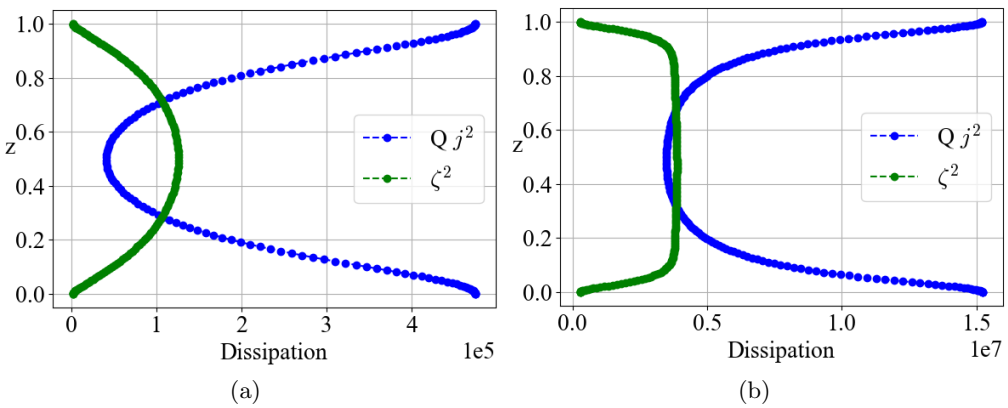

Figure 3.25: Plots of the horizontally averaged and time averaged dissipation plotted as a function of the vertical height of the simulation domain for two cases. (a) $Q = 2 \times 10^3$, $Ra = 1 \times 10^5$. (b) $Q = 2 \times 10^3$, $Ra = 1 \times 10^6$.

number as it may then represent an asymptote of the Nusselt number for very high Chandrasekhar numbers.

Related to the Nusselt number is the horizontally averaged temperature distribution shown in figure 3.23. The horizontally averaged temperature is nearly linear at the onset of convection, which for this graph occurs for $Ra = 1.53 \times 10^4$. The reason for this is that in the absence of convection, the heat diffusion equation has a linear solution. For higher Rayleigh numbers, figure 3.23 shows that, at the midplane of the simulation domain, the average temperature approaches a constant value, and the gradient of the average temperature at the boundary layer grows large. This temperature distribution is not unique to convection in magnetic fields.

An energy dissipation relation can be derived by taking the scalar product of velocity with the Navier-Stokes equation and averaging over the volume of the fluid. The result is

$$(Nu - 1)\,\frac{Ra}{Pr^2} = \langle \boldsymbol{\zeta}^2 \rangle + Q \langle \mathbf{j}^2 \rangle, \tag{3.14}$$

where $\mathbf{j} = \nabla \times \mathbf{b}$ is the current density and $\boldsymbol{\zeta} = \nabla \times \mathbf{u}$ is the vorticity. This equation describes the balance of energy dissipation within the flow. Physically, the left hand side represents the energy dissipated through the movement of heat, the term $\epsilon_v = \langle \boldsymbol{\xi}^{\mathbf{2}} \rangle$ is the dissipation of energy through viscosity, and $\epsilon_j = Q \langle \mathbf{j}^2 \rangle$ is the Ohmic heating. From this, the ratios of dissipation can be defined

as

$$\phi_j = \frac{\epsilon_j}{\epsilon_j + \epsilon_v}, \qquad \phi_v = \frac{\epsilon_v}{\epsilon_j + \epsilon_v}. \tag{3.15}$$

These ratios determine which mechanisms are dominant for energy dissipation and are shown in figures 3.24 (a) and (b) for the Chandrasekhar numbers $Q = 2\times10^3$ and $Q = 2\times10^6$, respectively. These figures demonstrate that the dissipation is governed by the Ohmic dissipation just after the onset of convection and that the Ohmic dissipation continues to be dominant, remaining about twice as large as the viscous dissipation. One possible reason for this is that the Lorentz force remains larger than the viscous force throughout the majority of the simulation domain as was shown in the balances section. Additionally, it is interesting that the ratios start to reach an asymptote before the mean flow dissipates; ϕ_v is never observed to exceed 0.4.

Also of interest is how the dissipation varies vertically, which is displayed in figures 3.25 (a) and (b). These figures show that the viscous dissipation is small at the boundaries whereas the Ohmic dissipation is large at the boundaries. In addition, the viscous dissipation becomes approximately constant in the center of the simulation domain for large values of the Rayleigh number, and the boundary layer of the viscous dissipation grows smaller for increasing Rayleigh number.

The reason the viscous dissipation becomes so small at the boundaries can be understood from the length scales. While the y-component of velocity is large due to the mean flow, the length scale of the y-velocity is the entire length of the simulation domain in the x-direction and z-direction, which makes these derivatives small. The x-component of the velocity also tends to have rather large length scales, like the y-velocity. On the other hand, the z-component of velocity has a much smaller length scale similar to the length scale of the temperature fluctuation in figure 3.1. This suggests that the z-component of velocity is responsible for the majority of the viscous dissipation. The z-component of velocity is zero at the boundaries, which explains why the viscous dissipation there is small. The turbulent regime does not have a mean flow, but the z-component of velocity is the dominant component of velocity which might explain why the viscous dissipation

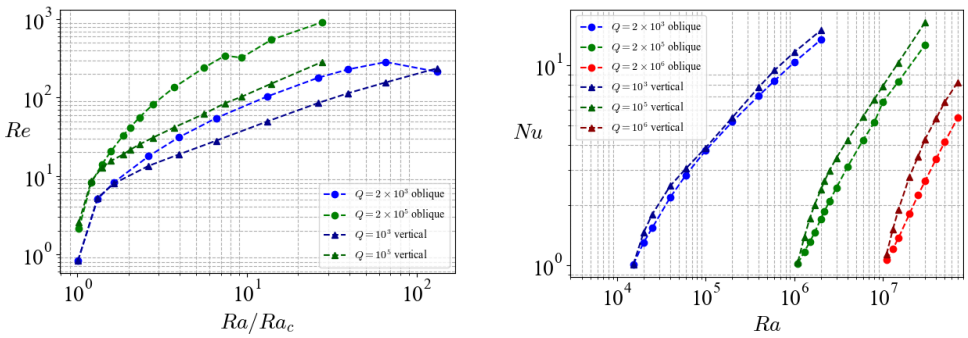

(a) (b)

Figure 3.26: Comparison of the Reynolds number and the Nusselt number between convection in a vertical magnetic field and convection in a tilted magnetic field. Data for vertical magnetic field from [4]. (a) Reynolds number. (b) Nusselt number.

is small near the boundaries for the turbulent regime.

The behavior of the Ohmic dissipation can be understood by taking the curl of equation 2.5, which yields

$$0 = \left(\cos\theta \frac{\partial}{\partial z} + \sin\theta \frac{\partial}{\partial x}\right) \boldsymbol{\zeta} + \nabla^2 \mathbf{j}. \tag{3.16}$$

The x and y components of vorticity are zero at the boundaries due to the boundary conditions, and the z-component of vorticity is small due to the length scales of the x and y components of velocity being large. The vorticity must therefore change rapidly near the boundaries to reach the large values in the center of the domain. This rapid change is encompassed in equation 3.16 in the term $\frac{\partial}{\partial z}\boldsymbol{\zeta}$ and must be balanced by the term $\nabla^2 \mathbf{j}$. If the length scale of current density does not change too greatly at the boundaries, the only way for equation 3.16 to be satisfied is for the current density to be large at the boundaries.

3.9 Comparison to convection in a vertical magnetic field

In this section, some comparisons are made to convection in a vertical magnetic field using data collected from [4]. The Reynolds number is compared in figure 3.26 (a) for two values of the Chandrasekhar number. The Reynolds numbers are similar at the onset of convection due to the Chandrasekhar numbers being compared having the same critical Rayleigh number. The Reynolds

number for the oblique magnetic field grows much faster than the Reynolds number in a vertical magnetic field for a wide range of Rayleigh numbers. This difference is due to the presence of a mean flow in the case of an oblique magnetic field that is not present for a vertical magnetic field. For the oblique magnetic field case $Q = 2 \times 10^3$, $Ra = 2 \times 10^6$, the mean flow dissipates and the Reynolds number falls to a similar value as observed in the case of a vertical magnetic field. This observation further supports that the mean flow is the reason for the large difference in the Reynolds number.

Figure 3.26 (b) shows the comparison between the Nusselt number for the vertical and oblique magnetic fields. The Nusselt number for the vertical magnetic field is larger than the Nusselt number for the oblique magnetic field and this difference is greater for larger values of the Chandrasekhar number. The mean flow may cause some of this difference since the mean flow and heat transport have an inverse relationship. However, even after the mean flow dissipates, the Nusselt number for convection in an oblique magnetic field continues to be smaller than the Nusselt number for convection in a vertical magnetic field, so this cannot be a complete explanation.

Chapter 4

Conclusion

This thesis has numerically investigated magnetoconvection with a tilted magnetic field for Chandrasekhar numbers of $Q = 2\times10^3$, 2×10^5, and 2×10^6. The highest Rayleigh number achieved was $Ra \sim 100Ra_c$.

Rayleigh-Bénard convection with an oblique magnetic field develops a mean flow for a wide range of both Rayleigh and Chandrasekhar numbers. This mean flow is governed by the averaged forces along the y-direction; in particular, the Reynolds terms determine the mean flow. These Reynolds terms are responsible for relaxation oscillations, and the reason $Q = 2\times10^3$ does not have relaxation oscillations is that the Reynolds term $\frac{\partial}{\partial x}\overline{(v'u')}^y$ is small. In addition, a thin boundary layer forms from the viscous and magnetic terms for simulations in which a mean flow is present, and this boundary layer was not observed for convection in a vertical magnetic field [4]. The presence of a thin boundary layer only in simulations with a mean flow suggests the mean flow is the cause of this boundary layer.

The mean flow causes the Reynolds number to be larger for convection in a tilted magnetic field than for convection in a vertical magnetic field [4]. The mean flow appears to inhibit heat transport, and the Nusselt number is smaller for convection in a tilted magnetic field than for convection in a vertical magnetic field. Unlike convection in a vertical magnetic field, there is no obvious power law scaling for the Reynolds number for convection in a tilted magnetic field [4]. The Nusselt number is bounded by $Nu = Ra/Ra_c$ for the values of Q studied in this paper, and future research could explore if this scaling holds beyond $Q = 2\times10^6$. The Ohmic dissipation is the

dominant form of energy dissipation for the parameter space studied in this paper. Perhaps future research could determine if the Ohmic dissipation remains dominant for higher Rayleigh numbers.

Given the relevance of the mean flow to the simulations in an oblique magnetic field, it would be worthwhile to develop an analytical model to predict the formation of the mean flow. Analytic expressions are often not derivable in fluid dynamics, but the formation of the mean flow for Rayleigh numbers just beyond the onset of convection suggests that it may be possible. In particular, the regularity of the spectra in figure 3.3 (a) suggests that the simulation for $Q = 2\times10^6$, $Ra = 1.04\times10^7$ can be described by weakly nonlinear theory. Using weakly nonlinear theory, future research could predict the formation of the mean flow and may give other predictions as well.

Magnetoconvection with a tilted magnetic field has several similarities to convection with a tilted rotation vector. In particular, Rayleigh-Bénard convection with a tilted rotation vector has convecting fluid structures aligned along the rotation vector, and mean flows form in convection with tilted rotation vectors [10]. These similarities suggest that symmetry breaking in Rayleigh-Bénard convection has a tendency to give rise to mean flows and tilted fluid structures.

Bibliography

[1] J.H. Thomas and N.O. Weiss. Fine structure in sunspots. Annu. Rev. Astron. Astr., 42:517–548, 2004.

[2] A.S. Brun and M.K. Browning. Magnetism, dynamo action and the solar-stellar connection. Living Rev. Sol. Phys., 14, 2017.

[3] M. Stefano, M.A. Calkins, J. Keith, and P. Marti. Magnetic quenching of the inverse cascade in rapidly rotating convective turbulence. Phys. Rev. Fluids, 4(4), 2019.

[4] Ming Yan, Michael A Calkins, Stefano Maffei, Keith Julien, Steven M Tobias, and Philippe Marti. Heat transfer and flow regimes in quasi-static magnetoconvection with a vertical magnetic field. Journal of Fluid Mechanics, 877:1186–1206, 2019.

[5] T. Al-Refae. Numerical simulations of convection with a horizontal magnetic field. Honors thesis CU Boulder, 2019.

[6] N.E. HurlBurt, P.C. Matthews, and M.R.E. Proctor. Nonlinear compressible convection in oblique magnetic fields. Ap. J., 457:933–938, 1996.

[7] N.E. HurlBurt, P.C. Matthews, and A.M. Rucklidge. Solar magnetoconvection. Sol. Phys., 192:109–118, 2000.

[8] S. Chandrasekhar. Hydrodynamic and Hydromagnetic Stability. Oxford University Press, U.K., 1961.

[9] Shaomeng Li, Stanislaw Jaroszynski, Scott Pearse, Leigh Orf, and John Clyne. Vapor: A visualization package tailored to analyze simulation data in earth system science. Atmosphere, 10(9), 2019.

[10] L. Novi, J. von Hardenberg, D.W. Hughes, A. Provenzale, and E.A. Spiegel. Rapidly rotating Rayleigh-Bénard convection with a tilted axis. Phys. Rev. E, 99, 2019.